

# Lawrence Berkeley National Laboratory

## LBL Publications

### Title

Depressurization-Induced Fines Migration in Sediments Containing Methane Hydrate: X-Ray Computed Tomography Imaging Experiments

### Permalink

<https://escholarship.org/uc/item/63z141s0>

### Journal

Journal of Geophysical Research: Solid Earth, 123(4)

### ISSN

2169-9313

### Authors

Han, Gyeol  
Kwon, Tae-Hyuk  
Lee, Joo Yong  
[et al.](#)

### Publication Date

2018-04-01

### DOI

10.1002/2017jb014988

Peer reviewed

# Depressurization-Induced Fines Migration in Sediments Containing Methane Hydrate: X-Ray Computed Tomography Imaging Experiments

Gyeol Han<sup>1</sup>, Tae-Hyuk Kwon<sup>2</sup>, Joo Yong Lee<sup>3</sup>, and Timothy J. Kneafsey<sup>4</sup>

<sup>1</sup> Department of Civil and Environmental Engineering, Korea Advanced Institute of Science and Technology (KAIST), Daejeon, South Korea, <sup>2</sup> Department of Civil and Environmental Engineering, Korea Advanced Institute of Science and Technology (KAIST), Daejeon, South Korea, <sup>3</sup> Oil and Gas Research Center, Korea Institute of Geoscience and Mineral Resources (KIGAM), Daejeon, South Korea, <sup>4</sup> Hydrocarbon Resources Program Head, Lawrence Berkeley National Laboratory, Berkeley, California, USA

## Abstract

Depressurization of hydrate-bearing sediments (HBS) can cause the movement of fine particles, and in turn, such fines migration affects fluid flow and mechanical behavior of sediments, ultimately affecting long-term hydrocarbon production and wellbore stability. This study investigated how and to what extent depressurization of HBS causes fines migration using X-ray computed tomography (CT) imaging. Methane hydrate was synthesized in sediments with 10% fines content (FC), composed of sands with silt and/or clay, and the hydrate-bearing samples were stepwisely depressurized while acquiring CT images. The CT images were analyzed to quantify the spatial changes in FC in the host sediment and thus to capture the fines migration during depressurization. It was found that the FC changes began occurring from the hydrate dissociation regions. This confirms that the multiphase flow caused by depressurization accompanies fines migration. Depressurization of HBS with a hydrate saturation of ~20–40% caused FC reduction from ~10% to ~6–9%, and the extent of fines migration differed with the particle sizes of the host sands and the types of fines. It was found that fines migration was more pronounced with coarse sands and with silty fines. Such observed level of FC reduction is estimated to increase sediment permeability by several factors based on the Kozeny-type permeability model. Our results support the notion that the extent of fines migration and its effect on fluid flow behavior need to be assessed in consideration of physical properties of host sediment and fine particles to identify optimum depressurization strategies.

## 1 Introduction

Natural gas hydrate reserves have received considerable attention as a potential alternative energy resource owing to their abundance and global distribution (Kvenvolden, 1993). Depressurization is considered to be one of the most promising methods for methane production from natural gas hydrate deposits (or hydrate production in the remainder of this paper) (Moridis et al., 2007). The depressurization is typically achieved by lowering the fluid pressure below the dissociation pressure at the prevailing temperature and salinity, where pore water is continuously pumped out from

target hydrate-occurring intervals in the production well (Makogon, 1997). This depressurization of hydrate-bearing sediments (HBS) not only causes multiphase fluid flows associated with hydrate dissociation, but also accompanies various emergent phenomena, including compression and mechanical failure of sediments (Kwon et al., 2013; Waite et al., 2010), sand production (Uchida et al., 2016), and fines migration (Jung et al., 2012; Lee et al., 2013)

Moreover, recent field-scale hydrate production tests (e.g., Malik in Canada and the Nankai Trough in Japan) have demonstrated that depressurization-based hydrate production can cause severe sand production and fines migration (Yamamoto et al., 2014). In particular, fines migration refers to a phenomenon in which fine sediment particles (or fines) that are smaller than sand particles ( $< 75 \mu\text{m}$ ) move along with the fluid in porous media. In turn, the fines migration can affect fluid flows in porous media and long-term hydrocarbon productivity, increasing permeability where displaced, or causing local pore clogging where deposited. Furthermore, it can also change sediment stiffness and strength and cause sediment failure around a wellbore, just as sand production does to wellbore instability (Moridis et al., 2011; Rutqvist et al., 2009). However, such transport behavior of sediment particles and its impact on gas production efficiency and wellbore stability remains poorly understood.

There have been extensive studies that explore the interactions among fluids, fines and pores to capture the dynamics of fines migration by physical experiments (e.g. Gabriel & Inamdar, 1983; Moghadasi et al., 2004; Muecke, 1979; Oyama et al., 2015; Pang & Sharma, 1997; Sharma et al., 1992; Valdes & Santamarina, 2006; Wan & Tokunaga, 2002) and by mathematical modeling (e.g. Bedrikovetsky, 2008; Bedrikovetsky et al., 2011; Bergendahl & Grasso, 2000; Cerda, 1987, 1988; Kampel et al., 2009; McDowell-Boyer et al., 1986; Shapiro et al., 2007; You et al., 2016). However, due to the complexities associated with hydrate dissociation, it is difficult to adopt these results directly into models to predict depressurization-induced fines migration. Only a limited number of studies have been performed that have investigated how and to what extent depressurization of HBS causes fines migration. Jung et al. (2012) firstly observed that the depressurization of gas hydrate caused fines migration in HBS prepared in a 30-cm long column. Murphy et al. (2017) performed physical modeling experiments on sand production from unconsolidated sediments, but without gas hydrate. In most physical experiments, the fines migration is typically examined by post-dissociation sampling, only providing the end-point result. This has been a bottleneck in examining such fines migration associated with fluid flows, hampering further progress.

Therefore, this study explored the fines migration induced by depressurization of HBS using X-ray computed tomography (X-ray CT) imaging. X-ray CT imaging is frequently deployed to observe the inner processes in HBS under high-pressure conditions, including hydrate

formation, dissociation, and gas production, (e.g. Abegg et al., 2007; Freifeld et al., 2006; Gupta et al., 2009; Kneafsey et al., 2007; Sell et al., 2016; Seol & Kneafsey, 2009; Ta et al., 2015). We prepared three different sediment samples composed of host sands with fine particles at controlled fractions. We then synthesized methane hydrates in those samples, and dissociated them by depressurization. During the step-wise depressurization, the hydrate-bearing specimens were periodically imaged using X-ray CT, and the obtained images were analyzed to monitor the temporal and spatial changes in the fines content in the host sediment during depressurization. Thereby, the extent of the fines migration is examined, and its implications to sediment permeability and gas hydrate production are further discussed.

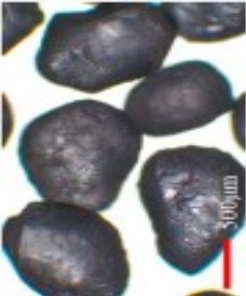
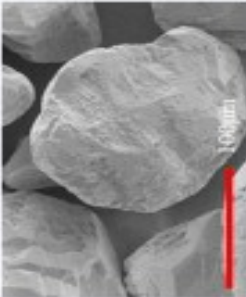
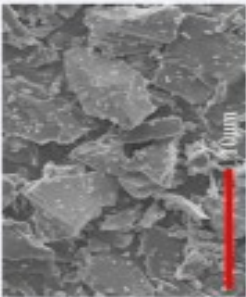
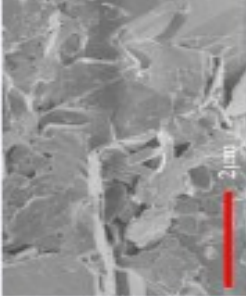
## 2 Materials and Methods

### 2.1 Materials

Fines migration is greatly affected by the relative size ratio between moving fine particles and the pore throats of host sediments. For comparison, we used two types of sands as host sediments: coarse sand (Ottawa 20-30, U.S. Silica, Frederick, MD, U.S.A.) with a mean grain size ( $D_{50}$ ) of 722  $\mu\text{m}$  and fine sand (F110, U.S. Silica, Frederick, U.S.A.) with  $D_{50}$  of 142  $\mu\text{m}$ . The fine sands were specifically chosen because their grain size distribution was close to that of sand-dominant sediments recovered from hydrate deposits in the Ulleung Basin offshore Korea (e.g., UBGH2-6B-22R, Cha et al., 2016). Silica silt and kaolinite clay were chosen as the fine particles; the silt has  $D_{50}$  of 20  $\mu\text{m}$  with a specific surface area less than 5  $\text{m}^2/\text{g}$  and no plasticity, while the kaolinite has  $D_{50}$  of 10  $\mu\text{m}$  with a specific surface area of 41  $\text{m}^2/\text{g}$  and low plasticity. Figure 1 shows the grain size distribution (GSD) curves, and Table 1 lists the physical and basic properties of the sediments used in this study. Methane gas with a purity of 99.9% (Gaskor, Asan, Daejeon, Republic of Korea) was used as a hydrate former, and deionized water was used to synthesize methane hydrate and to fully water-saturate the hydrate-bearing sediment samples.

Figure 1

Grain size distributions of the materials used: A Ottawa 20-30 sand, F110 sand, silica silt, and kaolinite, and b the sediment samples containing fines and the glass bead layer. The opening size of the screen is also denoted.

Parameter	Sand		Fines	
	Ottawa 20-30 sand	F110 sand	Silica silt	Kadinite
Soil type				
Mean grain diameter ( $\mu\text{m}$ )	722	142	20	10
Specific gravity	2.65	2.65	2.65	2.59
$e_{\text{max}} / e_{\text{min}}$	0.742/0.502 <sup>a</sup>	0.85/0.54 <sup>a</sup>	1.51/0.67 <sup>a</sup>	-
Plastic limit / Liquid limit	-	-	-	43/60
Void ratio of fines at 1 kPa	-	-	0.7	1.6
$e_{\text{ fines}}$	0.0031 <sup>c</sup>	0.016 <sup>c</sup>	0.67 <sup>c</sup> , 4.2 <sup>d</sup>	16 <sup>c</sup> , 41 <sup>d</sup>
Specific surface area ( $\text{m}^2/\text{g}$ )				
Particle shape image				

<sup>a</sup>Data were gathered from Cho et al. (2006). <sup>b</sup>The void ratio of fines at 1 kPa represents the void ratio under a free swelling condition for estimating the critical fine content, as suggested by Jung et al. (2012). <sup>c</sup>The specific surface area of the sand was calculated by assuming a sphere with the mean grain diameter. <sup>d</sup>The specific surface area of fines was measured by using BET method (dry method). <sup>e</sup>The specific surface area of fines was measured using the methylene blue adsorption method (wet method).

## 2.2 Experimental Apparatus

### 2.2.1 High pressure vessel

A high-pressure vessel with an inner diameter of 50 mm and a length of 611 mm was used for this study. The high-pressure vessel was composed of

three parts, as shown in Figure 2a: (from left to right) the inlet assembly; the X-ray transparent body, in which the sediments were placed; and the outlet assembly, through which methane gas was produced and fines were collected. The inlet and outlet assemblies were made of stainless steel (SUS316L), and the X-ray transparent body was made of aluminum alloy (AL7075). The outlet assembly had an empty space of 58 cm<sup>3</sup> to collect the migrated fines before the outlet fluid port, i.e., the collection space, and a stainless steel wire-wrapped screen was located between the sediment and the collection space to simulate wellbore conditions in field test production (Figure 2a). The wire-wrapped screen had a nominal opening size of 100 μm, which was smaller than the sand grain size but much larger than the fine particle sizes (silt and kaolinite); thus, the screen was designed to minimize the sand production.

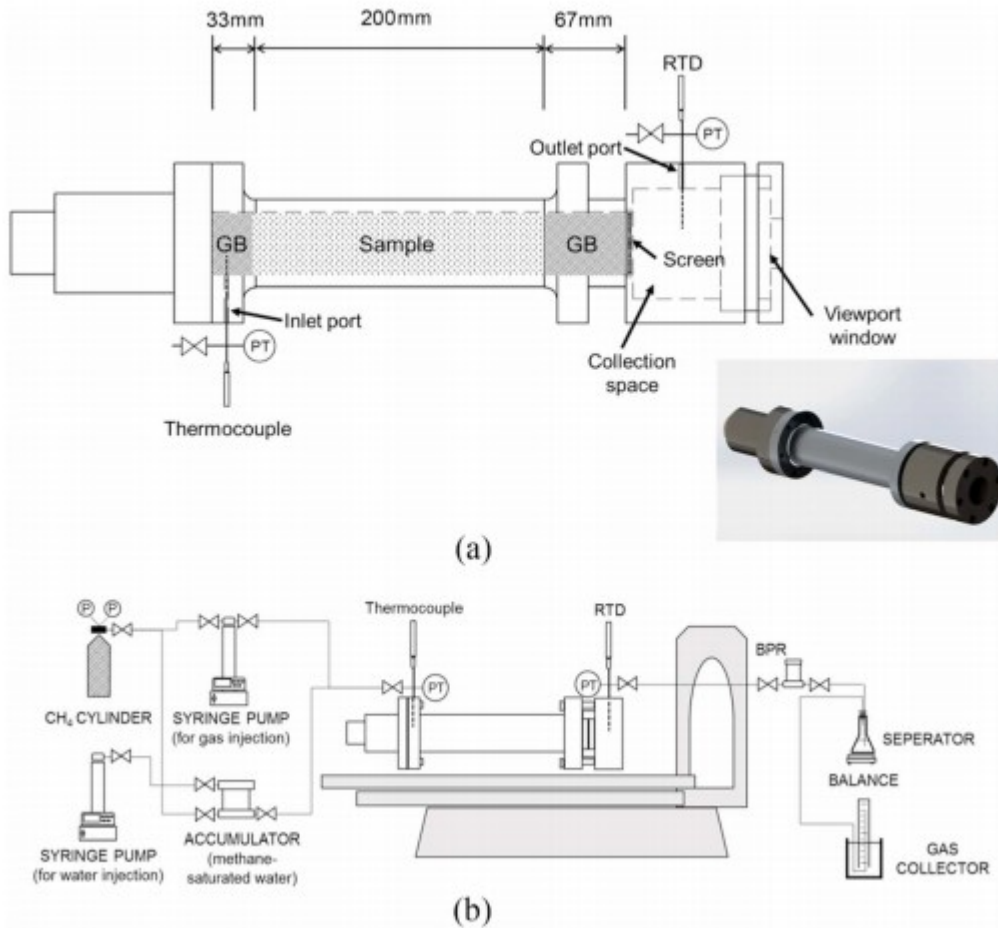


Figure 2

A a schematic drawing of the pressure vessel, and b the experiment setup for hydrate formation and dissociation with X-ray CT imaging.

In the well design practices, a gravel pack is generally installed to filter the sand production in addition to a screen. Herein, we compacted a 67–75 mm-long glass bead (GB) layer between the sediment and the screen as a gravel pack (i.e., outlet GB interval). The diameter of the glass beads ranged between 250 μm and 420 μm. Another 21–37 mm-long GB layer was also placed at the inlet side before the

sediment (i.e., inlet GB interval); these GB layers were kept dry during hydrate formation, such that no hydrate plugging was formed, facilitating the subsequent water injection process.

### 2.2.2 Instrumentation and X-ray CT imaging

Figure 2b shows the experimental set-up and instrumentation for synthesizing the hydrate-bearing sediments and conducting depressurization while imaging the samples using the X-ray CT scanner. The temperature of the vessel was controlled by circulating temperature-controlled fluid from the bath (RW-1025G, Jeio Tech, Daejeon, Republic of Korea) through the silicon tube wrapping around the vessel. A thermocouple (K-type, KMTSS-010-018, OMEGA Engineering, Stamford, CT, U.S.A.) and a resistance temperature detector (RTD, PT100, Hankook Electric Heater, Daejeon, Republic of Korea) were installed through the inlet and outlet fluid ports, respectively, to monitor the temperature inside the vessel. Two pressure transducers (Heise Model DXD Series, Ashcroft Inc., Stratford, CT, U.S.A.) were also installed at the inlet and outlet fluid ports to monitor the inlet and outlet pressures over the course of the experiments. The outlet fluid port was connected to a back-pressure regulator (BPR, Tescom 26-1700 Series, Emerson Electric Co., St. Louis, MO, U.S.A.) which controlled the outlet pressure during the depressurization processes. Produced fluids from the hydrate samples flowed to a separator, in which a balance measured the mass of water, and then the separated methane gas was collected by a gas collector.

In this study, an X-ray CT scanner (Optima CT660, GE Health, Little Chalfont, U.K.) was used for imaging the internal changes within the sediments over the course of the experiments. The CT provides spatially resolved quantitative information of the X-ray attenuation properties of the scanned region, which can be related to density via calibration. The data are typically displayed as 2-D or 3-D images. The scanning length was approximately 250 mm, such that the scan covered the whole length of the sediments and some GB layers. The time required for each scan was approximately 90 s, and such a short duration justified the assumption that no or minimal internal changes occurred during each scanning, allowing us to adequately capture the depressurization processes. The scanner had a maximum resolution of approximately 100  $\mu\text{m}$  and a minimum interval between slices (or slice thickness) of 625  $\mu\text{m}$ . All slice images obtained in our study comprised of  $512 \times 512$  pixels, with a pixel size of 107  $\mu\text{m}$  and a slice thickness of 625  $\mu\text{m}$ . The total number of slices was 380–400, which completely covered the sediments. The scanning was carried out with controlled current and voltage values of the X-ray source, i.e., 120 kV–210 mA, and 120 kV–250 mA. Pre-calibration tests were also conducted with known-density materials placed inside the high-pressure vessel to correlate the X-ray CT values and the density values (Figure S1 and Table S1).

### 2.3 Experimental procedure

The experimental procedure can be described with five steps: sample preparation (*Step I*), hydrate formation (*Step II*), water injection (*Step III*),

depressurization (*Step IV*), and post-experiment sampling (*Step V*). The representative P-T signature and X-ray CT images are shown in Figure 3. More details of these steps are described in the following sections.

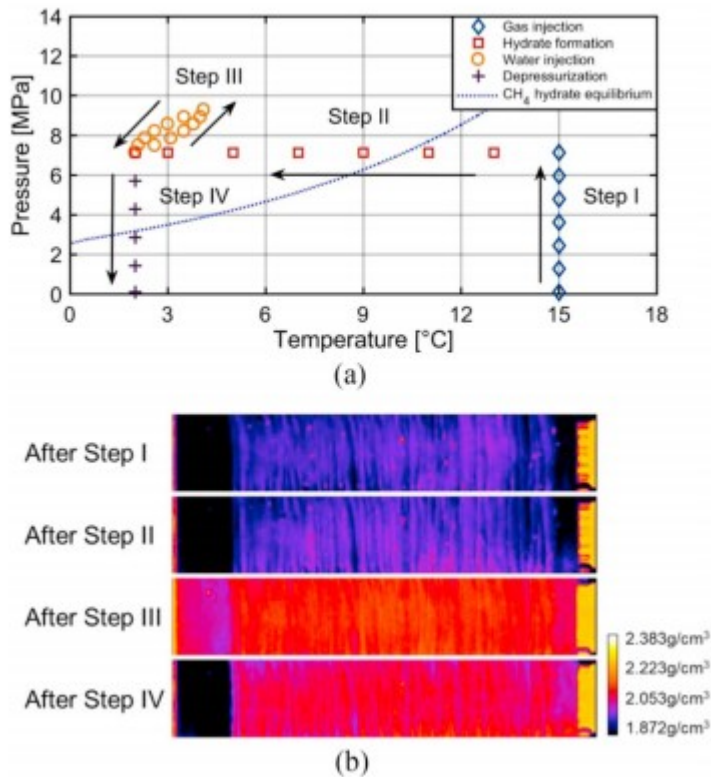


Figure 3

A pressure-temperature trace of the experimental procedure, and b representative X-ray CT images of sample 2.

### 2.3.1 Sample preparation

Three sediments were prepared by varying the type of host sands and fine particles: (a) Ottawa 20–30 sand with 9%w/w silica silt, (b) F110 sand with 11.5%w/w silica silt, and (c) F110 sand with 6%w/w kaolinite and 4%w/w silica silt. These three are referred to as Sample 1, Sample 2, and Sample 3 in the remainder of this paper, respectively. For all three samples, dry sand and dry fines were mixed in a plastic bag to achieve the fines content (FC) of approximately 10%, where FC was defined as the ratio of the mass of fine particles (of which particle size is less than 75  $\mu\text{m}$ ) to the total mass. At low FC where the fine particles do not displace host sediment grains and are not load-carrying, most of the fines can freely swell in the pores of host coarse-grained sediments. Accordingly, these fine particles in the pores of host sediments have their own natural porosity (or void ratio) under a free swelling condition, which is mainly controlled by pore water chemistry (Park & Santamarina, 2017). Thereby, the critical fine content ( $FC_{cr}$ ) for specific pore water chemistry can be defined as the FC at which pore spaces of the



host coarse-grained sediment are fully occupied by free swelled fines with a certain void ratio (Jung et al., 2012). The void ratios of free swelled silica silt and kaolinite with deionized water under no stress ( $e_{\text{fines}}$ ) are shown in Table 1, and the  $FC_{\text{cr}}$  of the samples are listed in Table 2. The initial FC was chosen to be approximately one third of the  $FC_{\text{cr}}$  for all the samples. The dry mixtures of the sediments were then pre-wetted with deionized water to achieve the pre-determined water contents. The initial water contents of Samples 1 and 2 was approximately 5%, and that of Sample 3, which contained kaolinite clay, was controlled to be approximately 10%, so as to provide a sufficient amount of water exceeding the liquid limit of kaolinite (Table 2). After thorough mixing with water, a certain amount of the pre-wetted mixture was sampled from the plastic bag, and its actual FC was then measured by wet-sieve analysis, and the initial FC ( $FC_{\text{ini}}$ ) was determined by averaging more than five measurements.

**Table 2**  
Initial conditions and basic properties of test samples

Soil property	Sample 1	Sample 2	Sample 3
Host sand	Ottawa 20–30	F110	F110
Fines	silt	silt	kaolinite+silt
Skeleton sand porosity <sup>a</sup>	0.34	0.41	0.44
Sample porosity <sup>b</sup>	0.26	0.35	0.38
Initial water content	5.0%	5.6%	10.2%
Initial fine contents, FC (< 75 μm)	8.8 ± 0.5%	11.5 ± 0.5%	10 ± 0.5%
Critical fine contents, $FC_{\text{cr}}$	32%	40%	36%
Pore saturation of fines, $S_{\text{fines}}$ <sup>c</sup>	21.4%	15.5%	14.3%
Sample length	20 cm	18.8 cm	20.2 cm
Length of the inlet GB layer	3.3 cm	3.7 cm	2.1 cm
Length of the outlet GB layer	6.7 cm	7.5 cm	7.5 cm
Sample diameter	5 cm	5 cm	5 cm
Pore saturation of water, $S_w$	36.9%	27.2%	44.5%
Hydrate conversion ratio <sup>d</sup>	48.4%	93%	47%
Pore saturation of hydrate, $S_h$ <sup>e</sup>	23–31%	32–44%	27%
Permeability <sup>f</sup>	$2 \times 10^{-12} \text{ m}^2$	$3 \times 10^{-13} \text{ m}^2$	$1 \times 10^{-13} \text{ m}^2$
Duration for hydrate formation	1.98 d	3.13 d	3.85 d
Water injection method	Flow-rate control (0.1–1 mL/min)	Flow-rate control (0.1–1 mL/min)	$\Delta P$ control (2.48 MPa)
Depressurization pressure step	0.35 MPa	0.35 MPa	0.7 MPa

<sup>a</sup>Skeleton sand porosity =  $(V_{\text{total}} - V_{\text{sand}} - V_{\text{fines}})/V_{\text{total}}$ . <sup>b</sup>Sample porosity =  $(V_{\text{total}} - V_{\text{sand}})/V_{\text{total}}$ . <sup>c</sup>Volumetric pore saturation of fines  $S_{\text{fines}} = V_{\text{fines}}/(V_{\text{total}} - V_{\text{sand}})$ , where  $V_{\text{fines}} = M_{\text{fines}}/G_{\text{sfines}}$ . <sup>d</sup>Conversion ratio = (Mass of water transformed into hydrate) / (total mass of water in sample pores). <sup>e</sup> $S_h$  was estimated from CT images. <sup>f</sup>The values represent the permeability of hydrate-containing and water-saturated sediment samples, which was measured after water injection before depressurization. During calculation, the permeability of the GB layers was assumed as  $1 \times 10^{-11} \text{ m}^2$ .

Prior to the compaction of each sample to the rigid-walled vessel, dry glass beads ( $\phi = \sim 35\%$ ) were first hand-tamped up to a pre-determined length (67–75 mm) on the wire-wrapped screen near the outlet port. Thereafter, each pre-wetted sample was hand-tamped within the rigid-walled vessel to a length of approximately 188–202 mm, and the porosity of the compacted samples ranged from 26 to 38%, and the porosity of host sand ranged 34 to 44%. Then, dry glass beads were again hand-tamped to a length of  $\sim 21$ –37 mm, filling the headspace up to the top of the vessel. After that, the inlet assembly was assembled to tightly hold the sediment. The specific lengths of these three regions for each sample are listed in Table 2. In this study, no additional effective confining stress was applied to the samples. Because the initial FC was as low as  $\sim 10\%$ , it was presumed that the fines were not load-carrying hence the effective stress had no or minimal effect on fines

migration. However, it should be noted that the stress and strain conditions can have a profound effect on the mobility of fines as the FC increases to a certain point where a significant portion of fine particles becomes load-carrying. Table 2 summarizes the initial conditions of the samples prepared in this study.

The vessel was flushed with methane gas for three pore volumes (or PV) at a low pressure of  $\sim 1.4$  MPa to remove air inside. Then, the vessel was pressurized to 6.9 MPa with methane gas by using a syringe pump (500D, Teledyne Isco, Lincoln, U.S.A.), and the ambient room temperature was kept constant at 15 °C. The vessel was kept for more than 24 hours until the volume of the injection syringe pump showed almost no change, indicating the complete dissolution of methane to pore water in the samples.

### 2.3.2 Hydrate formation

While feeding methane gas at a constant pressure of 6.9 MPa by using the syringe pump, the temperature of the vessel was lowered to approximately 2 °C to induce the formation of methane hydrate in the samples. Exothermal temperature peaks confirmed the nucleation of methane hydrate, and the hydrate formation lasted approximately 2–3 days until the injection rate of methane gas from the syringe pump to the vessel notably decreased. In addition, X-ray CT imaging was periodically conducted to monitor any change in the samples, and when there was no detectable change in time-lapsed CT images, the hydrate formation process was terminated. It is worth noting that the inlet and outlet GB intervals were kept dry, such that a minimal amount of methane hydrate was formed in the GB intervals during hydrate formation, facilitating the following water injection process.

### 2.3.3 Water injection

Upon the completion of the hydrate formation, the samples were flushed with methane-saturated water to remove free gas. This water injection was conducted to achieve the two-phase condition in the pore spaces with hydrate and liquid, simulating the oceanic hydrate conditions (Buffett, 2000; Davie et al., 2004; Xu & Ruppel, 1999). Prior to the injection, to minimize hydrate dissolution, deionized water was saturated with methane in the accumulator under 6.5 MPa and 8 °C, as shown in Figure 2b.

First, the initial injection was carried out at a flow rate of 0.1 ml/min for 0.5 PV to allow time for the injected water to be equilibrated with the vessel temperature as it wetted the inlet GB interval. Thereafter, the injection rate was elevated to 1 ml/min to minimize additional formation of hydrate inside the vessel. The propagation of the water front was monitored with the X-ray imaging. After the breakthrough of water at the outlet port, one more PV was flushed; during this flushing, permeability of the hydrate-formed and water-saturated sediment samples was roughly estimated from the pressure difference between the inlet and outlet ports, and the measured values are listed in Table 2. Then, the vessel was kept closed (i.e., no mass flux

condition) for more than 24 h. For Sample 3, the above injection rates were unattainable due to the presence of kaolinite and its low permeability; therefore, we imposed a constant pressure difference of 2.5 MPa between the inlet and outlet ports to complete the saturation process.

#### 2.3.4 Depressurization

Methane hydrate was dissociated by depressurization, where the pressure of the outlet port (or outlet pressure) was reduced by controlling the BPR while keeping the inlet port closed. The depressurization step was set to 0.34 MPa for Samples 1 and 2, and 0.68 MPa for Sample 3. X-ray CT images of the samples were acquired when the pressure was equilibrated in the samples after each depressurization step. During depressurization, all the produced fluids were first collected in the separator; the mass of water produced was measured using a balance, and thereafter, the volume of the separated methane gas was measured using a gas collector. This procedure was repeated until the outlet and inlet pressure reached atmospheric pressure level.

Over the course of depressurizations, the temperature was maintained at  $\sim 2$  °C for Samples 1 and 3, and at  $\sim 4$  °C for Sample 2, with some temperature fluctuation down to  $-1.5$  °C upon endothermic hydrate dissociation. The equilibrium pressure of methane hydrate at 2 °C with bulk water is 3.2 MPa (Sloan & Koh, 2008). When the pressure inside the vessel ( $P_{\text{vessel}}$ ) was higher than the equilibrium pressure ( $P_{\text{eq}}$ ), the depressurization was fairly straightforward. However, as  $P_{\text{vessel}}$  approached  $P_{\text{eq}}$  and methane hydrate began dissociating, the pressure equilibrium between the inlet and outlet (or stabilization) generally took more than 3 hours even for a small pressure drop of 0.34 MPa, and often no equilibrium was achieved for tens of hours (e.g., Sample 3) because of hydrate re-formation and hydrate plugging, blocking the pressure communication between the inlet and outlet part. In this case, we carried out X-ray CT imaging with such pressure difference while keeping no mass flux condition by closing the valves.

#### 2.3.5 Post-experiment sampling

Post-experiment sampling was conducted to measure the movement of fines in the sample upon the completion of depressurization. The sediments were carefully retrieved from the inlet side after disassembling the vessel. The inlet GB interval was sampled first, and the outlet GB interval was sampled last. For the sediment region, the sample was cut into several subsections with intervals of 2–3 cm. Then, these subsections (including the retrieved glass beads) were wet-sieved to analyze the remaining fines content (FC). The FC of each subsection was determined by using the average value from more than five samples; yet, the margin of error of the FC measurement was  $\pm 5\%$  because the sample volume was too small. As an example, the absolute error margin is approximated to be  $\pm 0.5\%$  if the measured FC is 10%.

### 3 Results

### 3.1 Hydrate formation

In all samples, overall increases in density were observed (Figure S2). The hydrate saturation and its local distribution in each sample were estimated by subtracting the baseline images (before hydrate formation) from the images after hydrate formation and before water injection; and the results are shown in Figure 4.

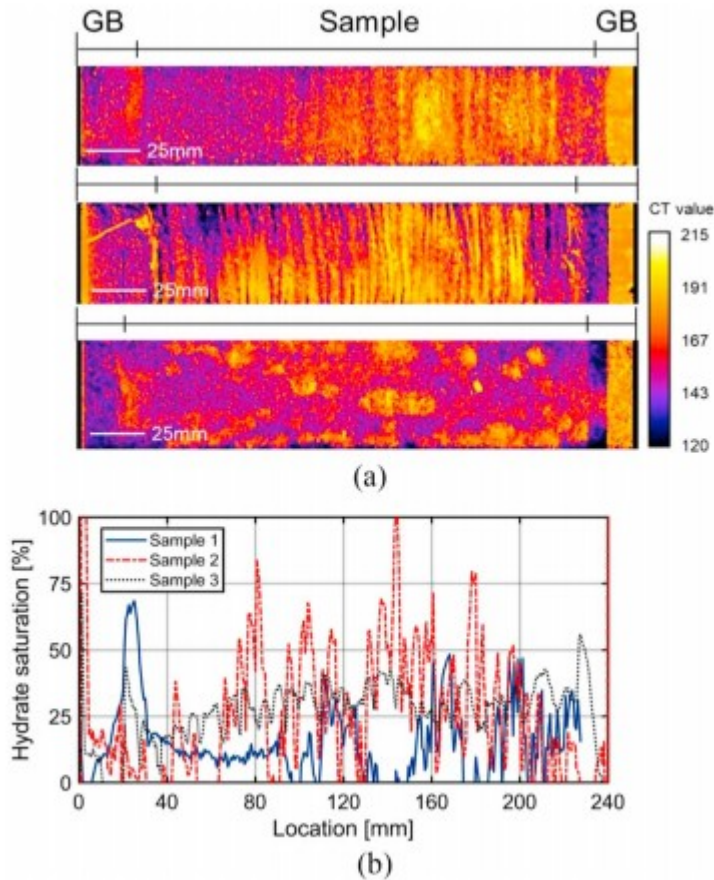


Figure 4

A the CT images of hydrate distribution in the tested samples. The x-y sliced images after hydrate formation were subtracted with their baseline images and they were stacked along the z-axis to highlight hydrate distribution in the samples. B the hydrate saturation profiles calculated from the CT images of the tested samples.

In Sample 1, the initial water content  $w_0$  and water saturation  $S_{w0}$  were approximately 5% and 37%, respectively, and the final hydrate saturation  $S_h$  was estimated to be ~23% based on the scanned X-ray images after 47 h of hydrate formation. The hydrate conversion ratio, which is defined as the mass of water transformed into hydrate divided by the mass of initial water, was ~48.4% based on CT images (Table 2). Assuming a hydration number of 6, the hydrate saturation  $S_h$  calculated from the injected methane volume was approximately 24.5%; this validates our  $S_h$  calculation from X-ray scanned images. In Sample 1, methane hydrate was quite uniformly formed with  $S_h = \sim 18\%$  in the first 7 cm region near the inlet port,

as can be seen in Figure 4. In the following region toward the outlet port, a heterogeneous distribution of methane hydrate was observed along the sample length, which was presumably attributed to capillary-induced water migration during hydrate formation (Kneafsey et al., 2011; Rees et al., 2011; Seol & Kneafsey, 2009).

In Sample 2, the initial water content  $w_o$  and water saturation  $S_{wo}$  were approximately 5.6% and 27%, respectively, and the final hydrate saturation  $S_h$  was estimated to be  $\sim 32\%$  based on the scanned X-ray images after 75 h of hydrate formation. The hydrate conversion ratio was  $\sim 93\%$  (Table 2). The hydrate saturation  $S_h$  calculated from the injected methane volume was approximately 35.1%; again, this supports our  $S_h$  calculation from X-ray scanned images. In Sample 2, methane hydrate was largely formed in the middle part of the sample (Figure 4).

In Sample 3, the initial water content  $w_o$  and water saturation  $S_{wo}$  were approximately 10.2% and 44.5%, respectively, and the final hydrate saturation  $S_h$  was estimated to be  $\sim 27\%$  based on the scanned X-ray images after 92 h of hydrate formation. The hydrate conversion ratio was  $\sim 47\%$  (Table 2). Notable patchy distribution of methane hydrate was observed in Sample 3, with  $S_h$  ranging from 20% to 50% (Figure 4).

The high hydrate conversion ratio of Sample 2 more than 90% was possibly attributed to the relatively uniform water distribution prior to hydrate formation. This in turn resulted in the most well-distributed hydrate in Sample 2 among the three samples. Contrarily, non-uniform water distribution in Sample 1 is presumed to have caused the low hydrate conversion ratio ( $<50\%$ ) because the capillary suction in Sample 1 was less than that in Sample 2 due to its large sand grain size. The low conversion ratio of Sample 3 ( $<50\%$ ) is thought due to the presence of adsorbed water on clay minerals, which were not frozen and transformed into hydrate.

In addition, slow injection of methane-saturated water into the hydrate-formed but gas-saturated samples at a low flow rate and such elevated pressure ( $\sim 7$  MPa) can cause additional hydrate formation. We back-calculated the hydrate saturation from the cumulative volume of methane gas produced upon the completion of depressurization, and the hydrate saturation was estimated to be approximately 31% for Sample 1 and 44% for Sample 2, which confirmed the additional hydrate formation. While such additional hydrate could have formed anywhere in the vessel, including in the GB layers as well as in the sediment sample, dissociation of hydrates that were formed in the GB layers is presumed to cause only minimal fines migration, if any, because there was no fines in the GB layers. Therefore, we assumed the hydrate saturation estimated from the produced methane volume as the upper bound, and the hydrate saturation estimated from the CT images before water injection as the lower bound, i.e.,  $S_h = 23\text{--}31\%$  for Sample 1 and  $S_h = 32\text{--}44\%$  for Sample 2 (Table 2). Whereas, all of the produced methane gas was not able to be collected for Sample 3 because

the hydrate plug was not fully dissociated even after depressurized to atmospheric pressure, as mentioned in the later section. Hence, we only provide the hydrate saturation for Sample 3, which was estimated from the CT images before water injection.

### 3.2 Depressurization

Step-wise depressurization was applied for the hydrate-containing sediment samples by controlling the outlet pressure, while monitoring the internal changes using X-ray CT imaging and collecting the produced gas and water. The X-ray images, the pressure traces, the volumes of produced gas and water, and the remaining fines content for all three samples are shown in Figures 5-7.

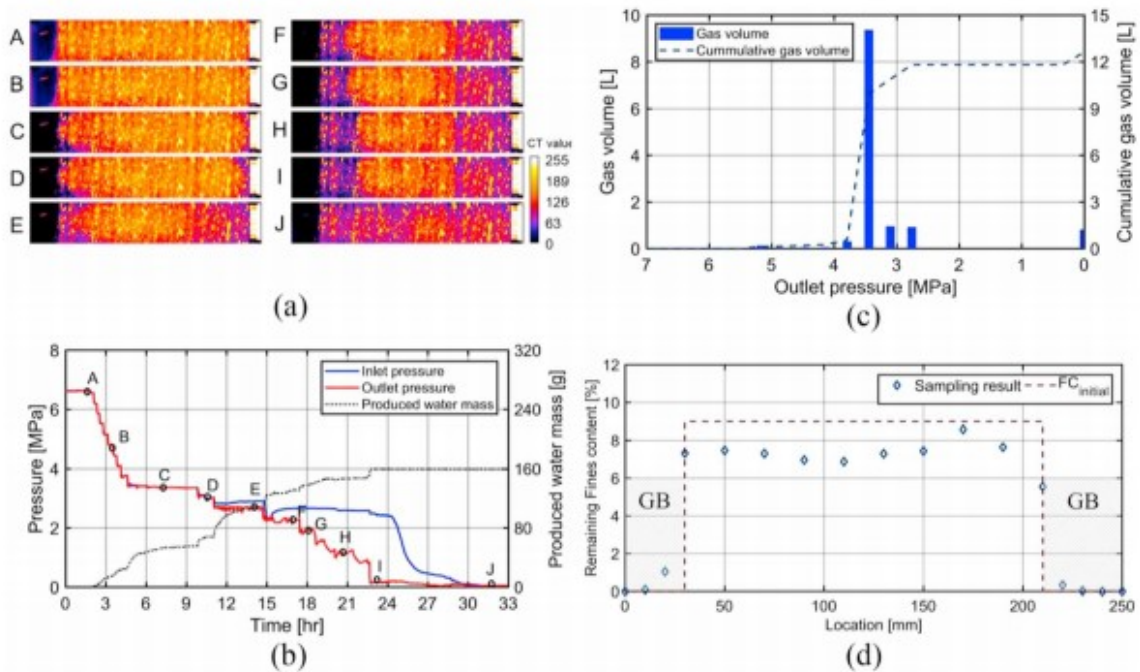


Figure 5

Depressurization result of sample 1: A the time-lapsed y-z sliced images, b the inlet and outlet pressure traces, c the collected gas volume during depressurization, and d the remaining fines content measured after experiment.



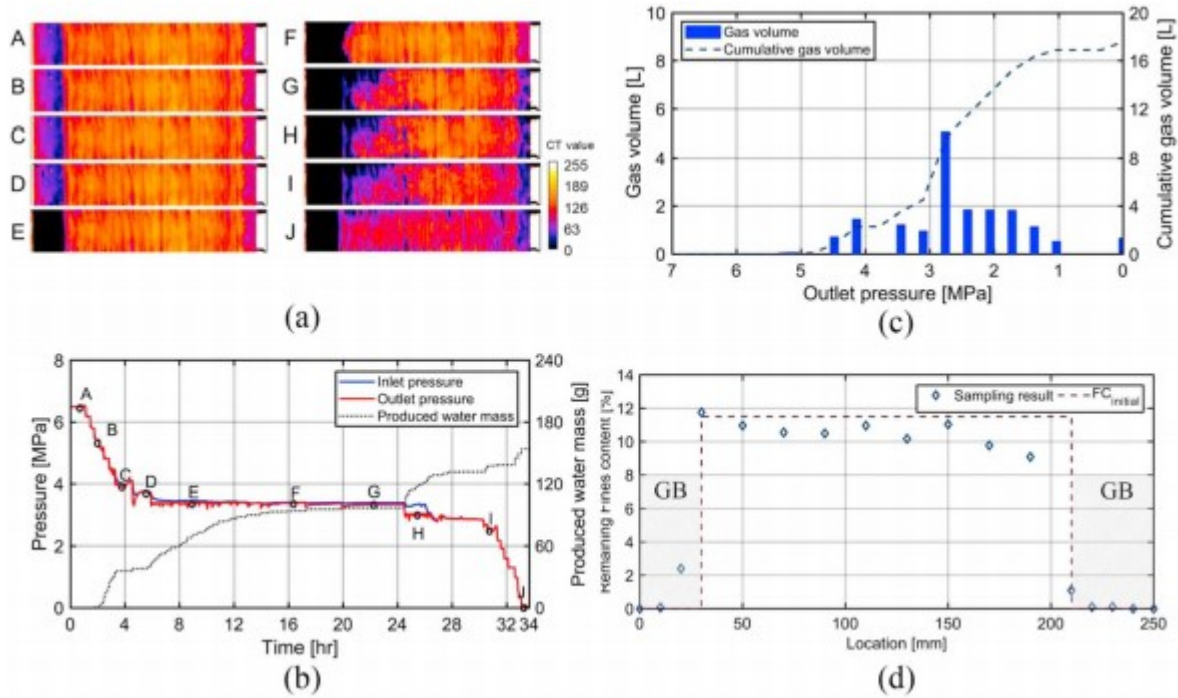


Figure 6

Depressurization result of sample 2: A the time-lapsed y-z sliced images, b the inlet and outlet pressure traces, c the collected gas volume during depressurization, and d the remaining fines content measured after experiment.

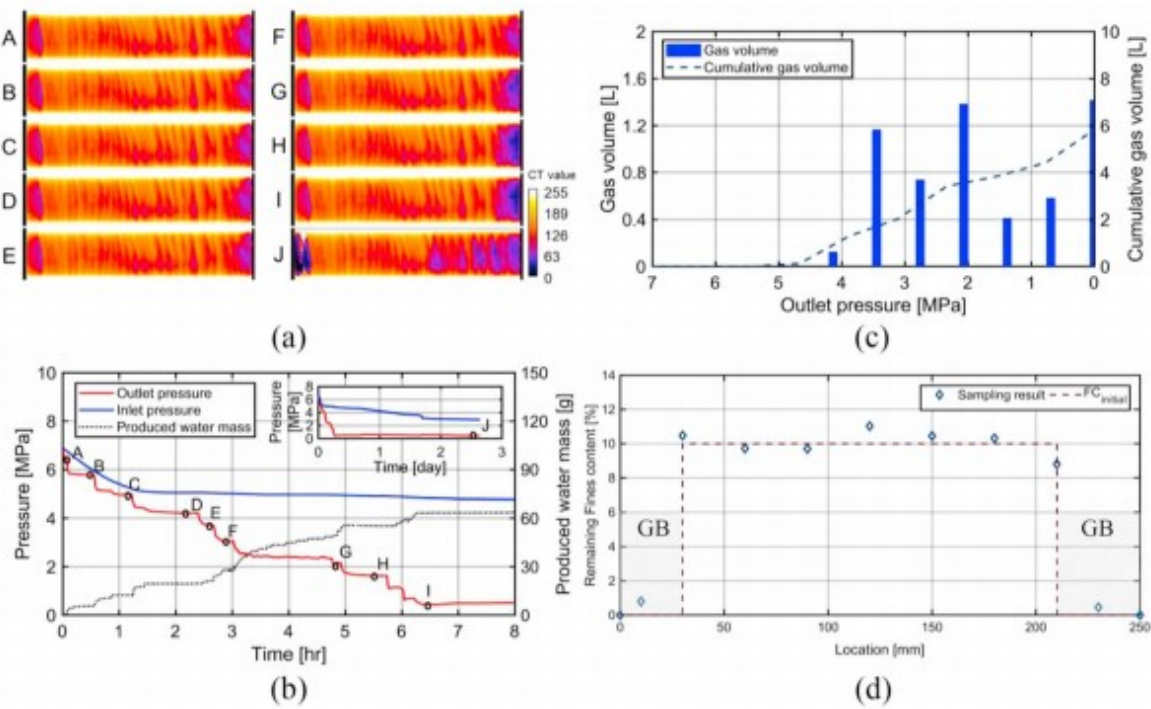


Figure 7

Depressurization result of sample 3: A the time-lapsed y-z sliced images, b the inlet and outlet pressure traces, c the collected gas volume during depressurization, and d the remaining fines content measured after experiment.

### 3.2.1 Sample 1 (Ottawa 20–30 sand and silt)

During the depressurization from 7 MPa to  $\sim 4.5$  MPa (Steps A–B, Figure 5), no dissociation occurred; thus, only small amounts of water and dissolved methane gas were produced with no or minimal changes in the obtained X-ray images. Methane hydrate began to be vigorously dissociated when the outlet pressure was lowered to  $\sim 3.5$  MPa (Step C, Figure 5), close to the equilibrium pressure for the sample's internal temperature of  $\sim 2$  °C. During this initial depressurization (Steps B–C), it was observed that preferential flow paths were created percolating from the outlet layer to the inlet GB layer along the rigid wall boundary (see Figure S3a). During the early stage of depressurization up to Step E, only minimal pressure difference was observed between the inlet and outlet, which also supports the presence of percolated flow paths with good pressure communication. Thereby, the dissociation fronts were developed both from near the inlet and outlet (Steps C–I, Figure 5a) though depressurization was imposed by controlling the outlet pressure with the inlet closed. Whereas, the pressure difference gradually increased from Step F and it became as large as  $\sim 2.5$  MPa at Step I, possibly attributed to re-formation of hydrate plugs. Due to this hydrate reformation, only a small amount of methane gas was produced for the depressurization from Step G to Step I. Thereafter, this differential pressure was gradually reduced, and the dissociation was completed at Step J. From I to J, some methane gas was also produced (Figure 5c), indicating that the hydrate plug which caused the differential pressure was dissociated. We observed that the remaining fines content in the sample was reduced from 9% down to  $\sim 6\%$  and the migrated fine particles were trapped in the inlet and outlet GB intervals (Figure 5d). Sample 1 contained the fine particles of  $\sim 75$  g, and among them 0.88 g fines migrated to the GB layers over the course of the depressurization; 0.55 g and 0.33 g of fine particles were trapped in the inlet and outlet GB layers, respectively.

### 3.2.2 Sample 2 (F110 sand and silt)

During the depressurization from 7 MPa to  $\sim 4.5$  MPa (Steps A–C, Figure 6), no distinctive changes in the obtained X-ray images were observed, with only a small amount of water and methane gas produced. Dissociation of methane hydrate was observed when the outlet pressure was lowered to  $\sim 3.5$  MPa (Step D, Figure 6) close to the equilibrium pressure for the temperature of  $\sim 2$  °C. Again, we observed that the dissociation fronts were developed from both ends (Steps F–I, Figure 6a), owing to the preferential flow paths along the rigid wall boundary (Figure S3b). Contrary to Sample 1, no significant pressure difference was observed, implying no hydrate reformed in Sample 2. Thereby, gas production was fairly continuous during depressurization to Step J, which differed from Sample 1. It was observed that the remaining fines content decreased from 11.5% to  $\sim 9$ –10%, with a



gradual reduction toward the outlet (Figure 6d). Sample 2 contained the fine particles of ~62 g, and among them 2.49 g fines migrated to the GB layers over the course of the depressurization; 1.48 g and 1.01 g of fine particles were trapped in the inlet GB layer and the outlet GB layers, respectively.

### 3.2.3 Sample 3 (F110 sand, silt and kaolinite)

During the depressurization from 7 MPa to ~4.5 MPa (Steps A–D, Figure 7), no dissociation occurred with no or minimal changes in the obtained X-ray images. Methane hydrate began to be dissociated when the outlet pressure was lowered to ~3.5 MPa (Step E, Figure 7). Similar to Sample 1, but more distinctively, the differential pressure between the inlet and outlet was developed from the beginning of the depressurization (Step A, Figure 7b). This indicates that the hydrate and fines already occluded pores even before depressurization, blocking the pressure communication between the inlet and outlet. Because of the hydrate plugging, the dissociation front started to develop from the outlet port. After ~10 h, the pressure difference became as large as ~4 MPa. After another ~50 h elapsed, this pressure difference was maintained at as large as ~3 MPa. Thus, we terminated the depressurization procedure at Step J, and lowered the inlet pressure by switching the back-pressure regulator to the inlet. There was a significant amount of gas produced during this pressure release from the inlet due to hydrate dissociation. This hydrate plugging phenomenon in Sample 3 presumably happened because of the kaolinite and silt mixture that were used as fine particles. This fine mixture would certainly cause more reduction in permeability compared to Sample 2, in spite of the similar mass fraction of fine particles. In hydrate dissociation experiments, it is often observed that some methane hydrate plugs remain *intact* for considerable amount of time, for example, tens of hours, even though one port or both ports are completely open to atmospheric pressure. In Sample 3, it was observed that the remaining fines contents near the inlet and outlet was reduced from 10% to 9–10%, but that the value in the central part showed minimal change. This indicates that only limited fines migration occurred, possibly attributed to the hydrate plugging. Although depressurization process of Sample 3 was rather complicated—the outlet pressure was first lowered and the inlet pressure was later lowered; the post-dissociation sampling revealed that 0.77 g and 0.88 g of fines were transported to the inlet and outlet GB layers, respectively, out of 67 g fines in the sample.

## 4 Analysis and Discussion

Depressurization of hydrate-bearing sediments leads to changes in sediment density and X-ray attenuation at a voxel scale (sub-mm scale); such density changes can be attributed to four underlying processes: movement of sand grains caused by a change in bulk sediment volume, replacement of hydrate crystals with water during dissociation, gas bubble generation, and fines migration (Figure S4).

Because the depressurization was conducted step-wise over a long time span (more than 24 h), we assumed that the fluid flow velocity was sufficiently low and only limited movement of sand grains occurred during depressurization, as corroborated by the CT images of the constant sample length before and after depressurization (Figure S5). The density change occurring when the hydrate crystals were replaced with water was relatively small because of the small difference in density between hydrate ( $\sim 0.9 \text{ g/cm}^3$ ) and water ( $\sim 1 \text{ g/cm}^3$ ), compared to the gas bubble generation or fine particle movement. Therefore, for a given voxel, the gas bubble generation and the fines migration are the major processes that can influence the X-ray attenuation and resulting CT value. In this section, with a-priori assumptions, the spatial evolution of free gas generation during depressurization was captured using CT images. Then, using the spatial information on gas bubbles, local changes in fines content during depressurization were tracked, which were compared to the post-experiment sampling results.

#### 4.1 Gas generation during depressurization

The generation and percolation of free methane gas was analyzed from the CT images (Figures 5-7). Figure 8 highlights the variations in histograms of CT values of the slice images for Sample 1 at some depressurization steps. As free gas was generated, the density and thus the CT values decreased overall. As an example of Sample 1, the median CT value was  $\sim 1610$  at Step B at the beginning of depressurization, but it decreased to  $\sim 1410$  at Step J when the depressurization was completed. Further, the CT values of the subtracted images from the baseline slice images (Step A) can be also plotted as a histogram, as shown in Figure 8, and this depicts the voxels of which the CT value was reduced. It can be assumed that the pixels having negative changes in CT values underwent reduction in density either because of the presence of generated gas bubbles or because of the removal of fine particles. On the other hand, it was noted that the CT value histogram of the subtracted images of Step B-A show a clear normal distribution ranging from  $-200$  to  $200$  with a center at zero. Given the fact that depressurization did not cause any hydrate dissociation from Step A to Step B, it is worth noting that this histogram implies a level of ambient noise from our X-ray CT imaging apparatus. Owing to this ambient noise in the images, labeling the voxels with decreased CT values as candidates containing gas bubbles can lead to overestimation.

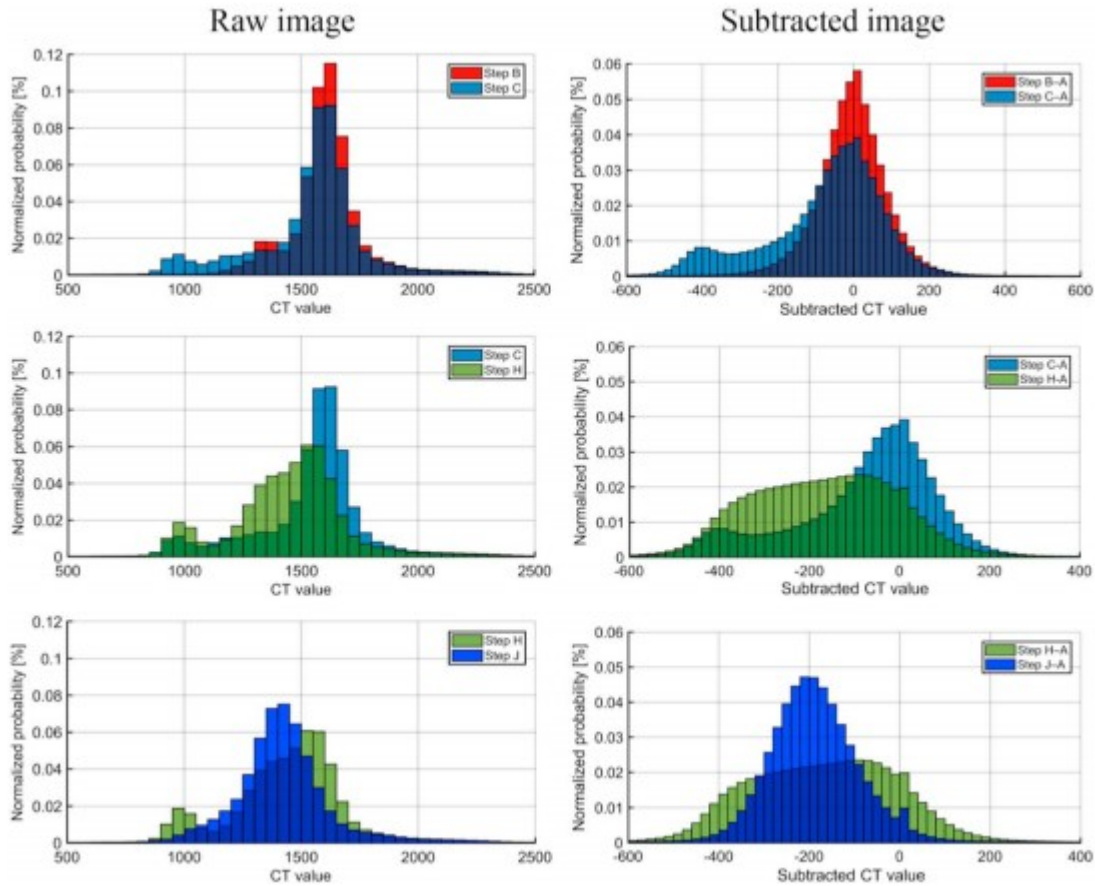


Figure 8

Variations in histograms of CT values of the sample 1 during depressurization.

To further filter out the voxels with gas bubbles (or gas voxels), we applied a threshold method by careful examining both histograms of the raw images and the subtracted images in Figure 8. At the beginning of the depressurization of Sample 1, the visible changes in the GB intervals can be noted due to the gas accumulation, which can be also confirmed in CT images B-C in Figure 5a. This corresponds to the increase in the number of voxels having CT values between 800 and 1200. In addition, from the histograms of the subtracted images, it was observed that the physical change occurring in the GB regions led to a CT value difference of more than 160. As depressurization proceeded further, the hydrate inside the sample gradually dissociated and created gas bubbles in the sample (Images C-H, Figure 5a). Accordingly, the number of voxels having a CT value between 1200 and 1540 increased, and variations in CT values were greater than 120, as shown in histograms C-H in Figure 8. On the basis of these observations, we chose voxels that had CT values less than 1540 and at the same time showed changes in CT value greater than  $-120$  as the ones with gas bubbles (or gas voxels), i.e., a threshold value of 1540 for the raw slice images and a

threshold value of  $-120$  for the subtracted images. As a result, Figure 9a shows the gas voxels for the steps of depressurization.

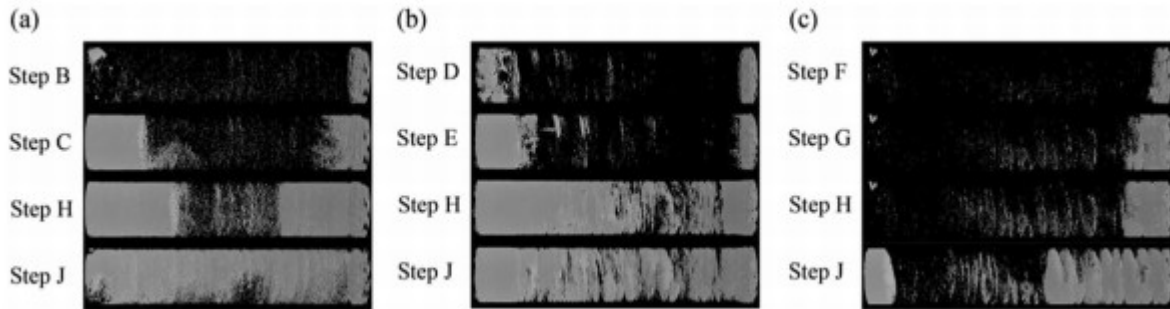


Figure 9

Evolution of gas bubbles generated during depressurization: A sample 1, b sample 2, and c sample 3. The white voxels indicate the ones with gas bubbles, and the black voxels with no gas.

We varied those threshold CT values with the samples. Following the same decision process, the threshold values for Sample 2 were chosen as 1340 for the raw slice images, and  $-120$  for the subtracted images. For Sample 3, the threshold values were chosen as 1400 for the raw slice images, and  $-80$  for the subtracted images (Figure S6). The results of the tracked gas for Samples 2 and 3 are depicted in Figures 9b and 9c, respectively. It can be clearly seen that the gas began nucleating from both ends, and the dissociation boundaries propagated inward as the depressurization proceeded. When depressurization and hydrate dissociation was completed in Samples 1 and 2 (Step J), it was found that the residual gas bubbles were evenly distributed over the sample, attributed to the expansion of gas volume by pressure reduction to an ambient pressure ( $\sim 0.1$  MPa), and the gas flow paths had percolated through the sample. Particularly, the gas pixels in Step J for Samples 1 and 2 illustrate the locations of the residual gas trapped by capillarity in a qualitative way. Whereas, for Sample 3, it should be noted that the hydrate plug was not dissociated up to Step J with the inlet pressure of  $\sim 3$  MPa. Because of such a hydrate plug, the gas paths had not fully percolated through the sample.

#### 4.2 X-ray image analysis of remaining fines content during depressurization

Periodic X-ray imaging during step-wise depressurization can be used to track the temporal variations in fines content along the sample, while post-dissociation sampling only provides end-point information. Over the course of sediment preparation through to hydrate formation to depressurization, one voxel can contain five components—sand, fine particles, water, methane hydrate, and free methane gas. Thus, in addition to the CT images obtained from the sample preparation stage and from the depressurization steps, the calculation of the mass of fine particles in each voxel requires some a-priori assumptions and additional information, including the produced water volume and the locations of gas bubbles (or gas voxels). The post-experiment sampling results were used for calibration. Herein, we assumed

no density difference between hydrate and water for simplicity, and that the total volume occupied by residual gas bubbles was the same with the volume of produced water at the very time step and these residual gas bubbles were uniformly distributed in the gas voxels. In examining the image set obtained at Step J of Sample 1 (Figure 5a), the voxel-scale analysis procedure is as follows:

1. Using the slice images obtained after gas injection (yet prior to hydrate formation, i.e., after Step I, Figure 3), the sand mass per voxel ( $M_{\text{sand}}$ ) can be obtained, assuming that water and fine particles were uniformly spread over the sample with the initial mixing ratios (water content  $w$  and fine content  $FC_{\text{ini}}$ ). This sand mass  $M_{\text{sand}}$  for each voxel is assumed to stay constant over the course of depressurization because the fluid flow rate by depressurization was as sufficiently low as  $\sim 3.2$  mL/min at the maximum.
2. From the slice images obtained at Step J, the bulk density of each voxel can be computed from its CT value; thus the total mass per voxel,  $M_{\text{total},J}$ , can be obtained. It is known whether a voxel has free gas or not (Figure 9). If a voxel contains gas, the gas volume per voxel ( $V_{\text{gas}}$ ) is assumed to be equal to the total volume of produced water divided by the number of gas voxels. Then, the total mass when the gas volume is replaced with water becomes  $M'_{\text{total},J} = M_{\text{total},J} + \rho_w V_{\text{gas}}$ . If it contains no gas,  $M'_{\text{total},J} = M_{\text{total},J}$  can be used as it is.
3. The void mass is defined as  $M_{\text{void},J} = M_{\text{fine},J} + M_{\text{water},J}$ , and this can be calculated by  $M'_{\text{total},J} - M_{\text{sand}}$ . The void volume  $V_{\text{void}}$  can be computed as  $V_{\text{void}} = V_{\text{total}} - V_{\text{sand}} = V_{\text{total}} - M_{\text{sand}} / (G_s \cdot \rho_w)$ , where  $G_s$  is the specific density of the sediment grain.
4. The void mass filled only with water ( $M_{\text{void}} = V_{\text{void}} \cdot \rho_w$ ) can be compared to the void mass  $M_{\text{void},J}$  thus,  $\Delta M = M_{\text{void},J} - M_{\text{void}} = M_{\text{fines},J} (1 - 1/G_s)$ . Therefore, the fines content (FC) at Step J can be computed as  $FC_J = M_{\text{fines},J} / (M_{\text{fines},J} + M_{\text{sand}})$ .
5. This fines content ( $FC_J$ ) is calibrated with the magnitude correction parameter  $\alpha$  and the offset parameter  $\beta$  (i.e.,  $FC_{J,\text{calibrated}} = \alpha \cdot FC_J + \beta$ ). The fitting parameters  $\alpha$  and  $\beta$  were determined by comparing the post-experiment sampling FC value with the average FC value of the corresponding section via the least-square fitting method. This voxel-scale analysis using the CT images was limited to the sediment sample region, excluding the GB layers at both sides. The calibrated FC results are shown in Figure 10.

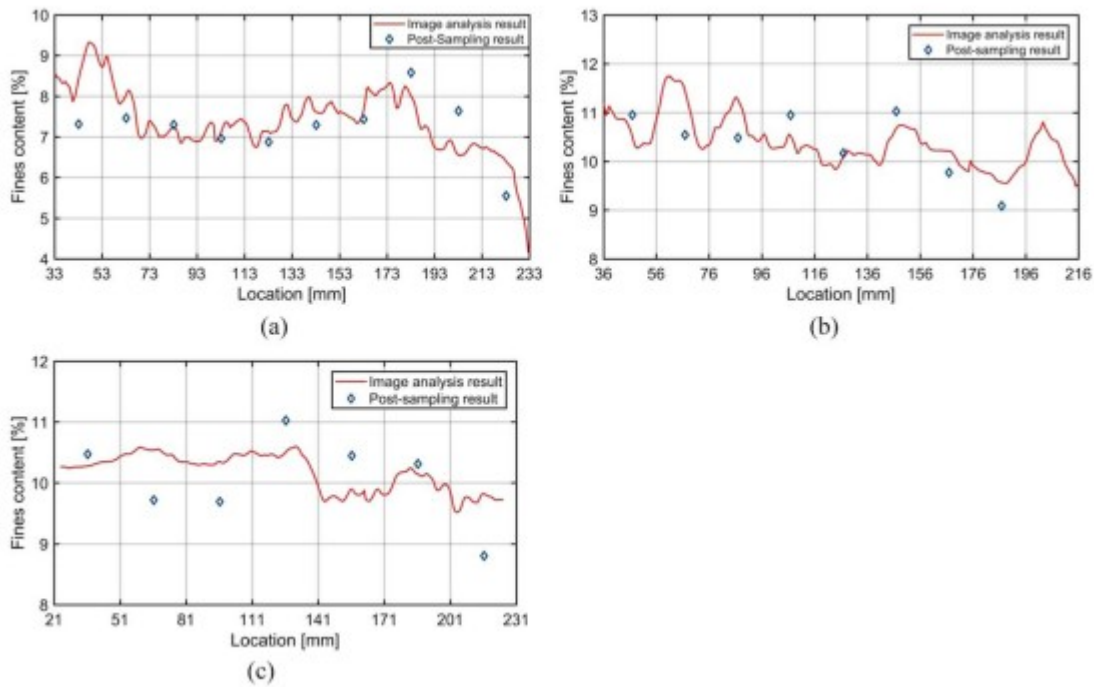


Figure 10

Remaining fines contents estimated from CT image analyses and post-sampling measurement after complete depressurization: A sample 1, b sample 2, and c sample 3. Note that the x-axis corresponds to the exact sediment length excluding the GB layers.

Table 3 summarizes this voxel-scale analysis procedure to estimate FC. The magnitude correction parameter  $\alpha$  of 0.35, 0.33, and 0.4 and the offset parameter  $\beta$  of 5.4, 6.8, and 4.1 appeared to result in the best fitting for Samples 1, 2, and 3, respectively. One of the main observations was that the gas saturation in the GB regions was higher than in the sediment region, owing to the larger pore sizes. Therefore, the gas voxels in the GB regions would contain more gas volume than the gas voxels in the sediment region; this led to an  $\alpha$  value of 0.3–0.4.

**Table 3**

Voxel-scale analysis procedure for fines content estimation

**Sample preparation (after step I)**

From image after gas injection but before, hydrate formation.

$$M_{\text{total0}} = M_{\text{sand}} + M_{\text{fines0}} + M_{\text{water}}$$

$$\text{Water content, } w = M_{\text{water}} / (M_{\text{sand}} + M_{\text{fines0}})$$

$$\text{Initial fines content, } FC_{\text{ini}} = M_{\text{fines0}} / (M_{\text{sand}} + M_{\text{fines0}})$$

$$M_{\text{sand}} = (1 - FC_{\text{ini}}) \cdot M_{\text{total0}} / (1 + w)$$

**Depressurization (After Step IV)**

From image after depressurization.

$$M_{\text{total}_j} = M_{\text{sand}} + M_{\text{fines}_j} + M_{\text{water}_j}$$

$$M'_{\text{total}_j} = M_{\text{total}_j} + \rho_w V_{\text{gas}}$$

$$M'_{\text{total}_j} - M_{\text{sand}} = M_{\text{void}_j}$$

$$M_{\text{void}_j} = M_{\text{fines}_j} + M'_{\text{water}_j}$$

$$V_{\text{sand}} = M_{\text{sand}} / G_s \rho_w$$

$$V_{\text{void}} = V_{\text{total}} - V_{\text{sand}}$$

$$M_{\text{void}} = \rho_w V_{\text{void}}$$

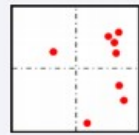
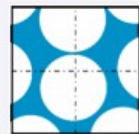
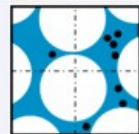
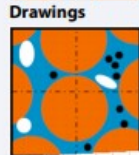
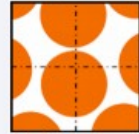
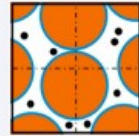
$$\Delta M = M_{\text{void}_j} - M_{\text{void}}$$

$$M_{\text{fines}_j} = \Delta M \cdot G_s / (G_s - 1)$$

$$FC_j = M_{\text{fines}_j} / (M_{\text{fines}_j} + M_{\text{sand}})$$

$$FC_j = (M'_{\text{total}_j} - V_{\text{total}} \rho_w) \cdot G_s / (G_s - 1) - M_{\text{sand}}$$

$$FC_{j\_calibrated} = \alpha \cdot FC_j + \beta$$

**Drawings****Drawings**

Even after correcting the FC values using  $\alpha$  and  $\beta$ , some local errors are seen in the result. In principle, the overestimation of FC is primarily due to the overestimation of gas volume. As mass compensation for such gas volumes becomes bigger, the total mass increases and results in higher FC. In addition, an increase in porosity (or reduction in dry density) of a host sediment due to loosened sand structure can lead to higher FC. On the other hand, the underestimation of gas volume causes underestimation of FC. For example, the estimated FC values in the inlet parts of Sample 1 (33–55 mm in Figure 10a) and Sample 2 (56–70 mm in Figure 10b) was overestimated compared to the sampling result. This is presumed attributed to the combination of the overestimation of gas voxels and the loosed host sand structure near the inlet GB region during depressurization. Meanwhile, the underestimation of FC in the 140–170 mm region of Sample 3 (Figure 10c) at Step J is presumed due to the underestimation of gas bubble volume as it is right next to the hydrate plug. Although the above image analysis was limited to the sediment sample regions, some deviations between the image analysis results and the post-sampling results were particularly noted near the GB layers, owing to the presence of the GB-sediment mixed zones. There were always transient mixed zones with a certain thickness at the GB-

sediment interfaces, which complicated the voxel-scale analysis to extract FC values. Caution should be taken when interpreting CT images near edges and boundaries where the image data can be easily contaminated by the neighboring materials.

#### 4.3 Changes in fines content caused by depressurization

From the image sets obtained during depressurization, one-dimensional profiles of the change in fines content in the sample can be computed, and the results are shown in Figure 11. The variations were calculated by subtracting the FC value at the initial step (Step A) from the FC value at each step in question, i.e.,  $\Delta FC_{j-A} = FC_j - FC_A$ , where the subscripts j and A indicate the depressurization step at the time in question and Step A, respectively. In Sample 1, initial depressurization caused the hydrate dissociation from both ends due to the presence of preferential flow paths (Step C, Figure 5, Figure S6a, and Figure 9a). At the same time, it was observed that the change in FC values near the inlet and outlet became negative first, associated with the development of hydrate dissociation fronts (Figure 11a). Because the middle part of the hydrate-bearing sample was much less permeable than the GB layers, the fluids released from hydrate dissociation flowed readily toward the GB layer. Therefore, such fluid flows from the dissociated regions to the neighboring GB layer dragged and pushed the fine particles to the inlet and outlet GB layers. Thereafter, the subsequent depressurization caused further reduction in FC associated with the gradual propagation of hydrate dissociation front toward the sample center (Steps C-F, Figure 5, Figure 9a, and Figure 11a). The post-dissociation sampling result from the GB layers, in which the significant FC value (~1%) were particularly found in the inlet GB layer, confirms the observed fines migration toward both ends (see Figure 5d). Shortly thereafter, as the gas path percolated from Step H, the hydrate remaining in the middle region (80–160 mm in Figures 5a and 11a) became readily dissociated, which led a significant reduction in FC in that region (Steps F-J). Although it is challenging to reveal the migration direction or path of the fine particles from the images, it would be reasonable to assume that majority of the fines in this middle region primarily migrated toward the outlet. Given the fact that the inlet pressure was kept consistent while the outlet pressure decreased, it is because dissociated fluids primarily flowed toward outlet with gas bubbles expanding during the depressurization from Step H to Step J. This also led to more FC reduction near the outlet, as shown in the FC profile at Step J in Figure 11a. This observation provides a clear evidence that the direction of fines migration is heavily influenced by the flow directions of multiphase fluids released from gas hydrates and the boundary conditions.



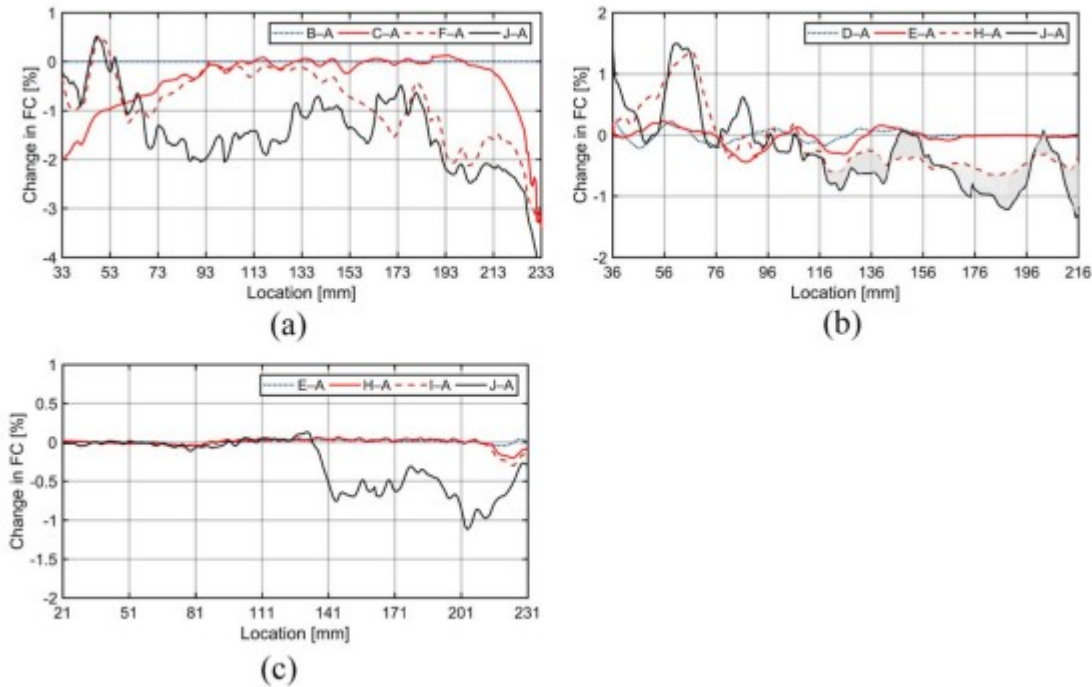


Figure 11

Changes in fine contents (FC) during depressurization: A sample 1, b sample 2, and c sample 3. Note that the x-axis corresponds to the exact sediment length excluding the GB layers and that the hatched zones indicate the migrated fines compared to the previous step.

In Sample 2, fines migration was more pronounced toward the outlet though the extent of  $\Delta FC$  was less than that of Sample 1. The FC value stayed consistently during the initial depressurization until Step E. As the pressure was gradually reduced to less than 3 MPa (from Step E to Step J; Figure 6), rigorous hydrate dissociation produced a significant volume of gas through the outlet port, and the FC near the outlet GB layer (i.e., the 96–216 mm region) began to decrease in response to such large gas flow. It is worth noting that the local movement of fine particles is well captured in this study, as depicted by the hatched areas in Figure 11b. Meanwhile, slight increases of FC by  $\sim 1\%$  was observed near the inlet (i.e., the 56–76 mm region; Steps H and J, Figure 11b). Similar to Sample 1, such fines migration toward the inlet GB layer as well as the outlet GB layer was partly attributed to the dissociation occurred from the both ends during the early stage of hydrate dissociation. This is corroborated by the post-dissociation sampling result, in which we found that the FC in the inlet GB was greater than 2% and the FC at the transient region between the sample and the inlet GB layer was  $\sim 12\%$  which was slightly higher than the initial FC ( $\sim 11.5\%$ ). In addition to that, it is possible that the observed FC increase near the inlet was partly due to the loosened sand structure caused by hydrate dissociation under no confining stress, though this could hardly be captured by the CT images of the sample.

In Sample 3, hydrate dissociation was constrained to the region near the outlet due to the existence of hydrate plugging. Therefore, only minimal

changes in FC profiles were found during depressurization up to Step H, as shown in Figure 11c. Thereafter, the gradual propagation of hydrate dissociation front into the center was accompanied with the fluid flows toward the outlet, and this led to the notable reduction in FC in the second half of the sample near the outlet (Steps I-J, Figure 11c). Because there was no hydrate dissociation in the first half due to the hydrate plug, the fines migration was not observed in such a region, which is corroborated by the location of gas voxels (Figure 9c).

#### 4.4 Implication for gas hydrate production

It was again confirmed that the particle size of the host sand had a significant effect on the extent of fines migration; as the host sediment particle size increased, more fines migration occurred. The mean particle size of the host sand of Sample 1 was approximately 720  $\mu\text{m}$ , and the resulting change in FC in Sample 1 ranged approximately from 2 to 4% out of 9% initial FC for  $S_h = \sim 20\text{--}30\%$ . In contrast, the host sand of Sample 2 had the mean size of approximately 140  $\mu\text{m}$ , and the change in FC in Sample 2 was approximately 1–2% out of 11.5% initial FC for  $S_h = \sim 30\text{--}40\%$ . In both samples, the fine particles were non-plastic silts with small specific surface area. In Sample 3 which had the same host sand as Sample 2, there was approximately 0.5–1% FC change out of the 10% initial FC for  $S_h = \sim 30\%$ , which occurred only over half of the sediment due to the hydrate plug.

Exceptionally, Sample 3 had a hydrate plug that caused remarkably slow dissociation and also retarded the pressure equilibrium between the inlet and outlet pressures. Although the host sands and the fines contents were the same, the baseline permeability of Sample 3 was  $\sim 10^{-13} \text{ m}^2$ , significantly lower than the other two samples due to the presence of kaolinite. Hence, it is presumed that the presence of kaolinite and the low baseline permeability facilitated the pore-plugging by hydrate formation prior to depressurization.

The gravel pack used in this study, composed of glass beads having a particle size of 250–420  $\mu\text{m}$ , effectively captured all migrated fine particles in all experiments; thus, there was a limited amount of fines produced through the outlet fluid port. Therefore, silt-sized fine particles ( $D_{50} = 20 \mu\text{m}$ ) can be effectively filtered using the gravel pack with such sizes. Because of  $D_{15\_gravelpack} = 250 \mu\text{m}$ ,  $D_{50\_gravelpack} = 300 \mu\text{m}$ ,  $D_{50\_fines} = 20 \mu\text{m}$ , and  $D_{85\_fines} = 50 \mu\text{m}$ , the gravel pack satisfies the filter specifications by the U.S. Army Corp, where  $D_{15\_gravelpack} / D_{85\_fines} < 5$  and  $D_{50\_gravelpack} / D_{50\_fines} < 25$  is suggested (Sherard et al., 1984). Meanwhile, it has been reported that particle clogging occurs when the ratio of opening size (i.e., equivalent to pore size) to particle size (i.e.,  $D_{50\_fines}$ ) is less than 3 (Valdes & Santamarina, 2006). If the pore size is assumed to be 20% of  $D_{15\_gravelpack}$ , the pore size of the gravel pack is  $\sim 50 \mu\text{m}$  and  $D_{50\_fines}$  is 20  $\mu\text{m}$ . This also supports that the mobile silt particles were readily trapped at the gravel packs in this study.

It was observed that most fines migration occurred in areas where hydrates dissociated and gas bubbles generated, and the area with fines migration gradually expanded as hydrate dissociation front propagated from the boundary to the center of the sample. It indicates that fluid flows caused by hydrate dissociation dragged and pushed fine particles. In particular, such fines migration became pronounced with a significant gas production when the pressure was reduced to less than the equilibrium pressure. This implies that depressurization of hydrate-bearing and coarse-grained sediments can cause considerable fines migration for the condition where the target formation contains some fine particles;  $\Delta FC = \sim 1\text{--}4\%$  out of 10% initial FC for  $S_h = 20\text{--}40\%$  in our cases. This FC change observed in our study is remarkably consistent with the results reported by Jung et al. (2012); they observed the fines removal with the average  $\Delta FC$  of  $\sim 1\%$  out of 5% initial FC for  $S_h = 27\%$ , where a kaolinite-sand mixture with 5% FC was used as the host sediment, pre-wetted and saturated with deionized water. Although there were differences in between  $\text{CH}_4$  hydrate and  $\text{CO}_2$  hydrate and between the initial FC values ( $\sim 10\%$  in this study versus  $\sim 5\%$  in their study), the other influencing factors were in the similar ranges, e.g., the hydrate saturation ( $S_h = 20\text{--}40\%$ ), the sample length ( $\sim 20\text{--}30$  cm), and the sand particle size ( $D_{50} = \sim 140$   $\mu\text{m}$ ). This allowed proper comparison with our results, and it reveals that depressurization of HBS with a low initial FC of 5–10% and intermediate hydrate saturation  $S_h = 20\text{--}40\%$  can cause considerable fines migration, reducing FC by 1–2% in average and up to  $\sim 4\%$  locally.

As sandy formations with high hydrate saturation are targeted for gas production using depressurization, we expect fines migration to occur. There are many natural sediments of concern: coarse-grained sediments with  $S_h > 30\%$  cored in hydrate deposits show FC values ranging from  $\sim 5\%$  to  $\sim 20\%$  (e.g., 5–8% of FC in Mallik2L-38 Core 18, Canada;  $\sim 30\%$  of FC in D-GH, Mt. Albert, Alaska;  $\sim 20\%$  of FC in NGHP-01-10D, India;  $\sim 32\%$  of FC in U1326D-7X-1, Cascadia margin;  $\sim 30\text{--}40\%$  of FC in AT1-C-8P, the Nankai Trough; 22% of FC in UBGH2-6B-22R and 2.4% in UBGH2-5B-22H in Ulleung Basin; data gathered from Cha et al., 2016; Collett et al., 1999; Ito et al., 2015; Torres et al., 2008; Winters et al., 2014). For a sand layer with high  $S_h > 60\%$ , the FC change can be greater than the values observed in our study. Even after complete hydrate dissociation, as the fluids from far field will flow into a wellbore through near-wellbore sediment layers, such continuous fluid flows can cause fines migration to a greater extent than we observed.

The fines migration has a pronounced effect on transport properties of sediments. In particular, the reduction in fines content or removal of fines can increase the sediment permeability. The order-of-magnitude estimation on permeability change by the fines removal can be conducted using one of the widely used Kozeny family of permeability models (Carman, 1937; Kozeny, 1927; Scheidegger, 1960):

$$K = \frac{C}{\tau^2 S_s^2} \frac{\phi^3}{(1 - \phi)^2}, \quad (1)$$

where  $C$  is the empirical shape factor,  $\tau$  is the tortuosity ( $= L_a/L$ ; defined as the average length of the fluid path  $L_a$  divided by the geometrical length of the sample that fluid flows through  $L$ ),  $S_s$  is the specific surface area per sediment grain volume, and  $\phi$  is the sediment porosity. In an ideal condition with the FC significantly less than the critical FC, where fine particles are uniformly and homogeneously disseminated in host sand pores, not occluding any pore throat, it can be assumed that the skeletal structure composed by sand particles determines the flow paths (hence the tortuosity) while the fines contribute to the frictional drag (hence the specific surface area). In such case, the sediment permeability is known to be sand-controlled (Jung et al., 2012). As the initial FC tested herein ( $\sim 9$ – $12\%$ ) was much less than the critical FC ( $\sim 30$ – $40\%$ ), the sediment permeability is presumed to be in the regime of sand-controlled permeability. For sand-controlled permeability with low FC, assuming the constant empirical shape factor  $C$  and the constant tortuosity  $\tau$ , the permeability relative to the baseline permeability  $K_r$  can be expressed as follows:

$$K_r = \frac{K}{K_o} = \frac{S_{s0}^2}{S_s^2} \frac{\phi^3 (1 - \phi_o)^2}{\phi_o^3 (1 - \phi)^2}, \quad (2)$$

where

$$\phi = \phi_{sk} - \left( \frac{FC}{1 - FC} \right) \cdot (1 - \phi_{sk}), \quad (3)$$

and

$$S_s = S_s^{sand} \cdot (1 - FC) + S_s^{fine} \cdot FC. \quad (4)$$

Herein, FC is the fines content, and  $\phi_{sk}$  is the skeleton porosity when fines are completely removed without changing the bulk volume. As an order-of-magnitude estimate, the case of Sample 2 can be modeled with the skeleton porosity of 0.42, the specific surface area of the sand  $S_s^{sand}$  as  $42400 \text{ m}^{-1}$ , and the specific surface area of the fines  $S_s^{fine}$  as  $1.1 \times 10^7 \text{ m}^{-1}$  (Table 1). When the initial FC is 10%, the removal of 1–4% FC will increase the permeability by the factors of 1.3–3.6. Our order-of-magnitude estimate reveals that the complete wash-out of 10% FC can increase the permeability by three orders of magnitude. Therefore, the fines migration may help fluid flows during hydrate production if there is no clogging by migrated fines, or it may develop fast and preferential flow pathways around a production well. On the other hand, migrated fines can occlude local pores and cause problems in gravel packs and near-wellbores (Miranda & Underdown, 1993). The extent of fines migration and its effect on fluid flow behavior and wellbore stability needs to be assessed in consideration of the physical

properties of the host sediment and fine particles to identify optimum depressurization strategies.

Lastly, fines migration is controlled by several factors, including flow velocity, multiphase flow, relative size ratio of fine particles to pore sizes of host sediments, physico-chemical characteristics of fines, and pore water chemistry (Jung et al., 2012, 2017; Sharma et al., 1992; Valdes & Santamarina, 2006; Wan & Tokunaga, 2002). When fines are predominantly clayey minerals with high specific surface area, the inherent behaviors of fines are dominated by pore water chemistry as the salt and pH control their fabrics (Mitchell & Soga, 2005; Van Olphen, 1963). In the presented study, silica silt and kaolinite were used as fines and de-ionized water as pore water in order to examine the physical interplays between depressurization-induced hydrate dissociation and fines migration, excluding any complicated effect by pore water chemistry. The results obtained in this study will provide baseline experimental data for further in-depth analyses of fines migration during gas production from hydrate reservoirs though the impact of pore water chemistry and their interplays with clayey fines on fines migration still warrants further investigation.

## 5 Conclusions

This paper presents core-scale experimental results on depressurization-induced fines migration in methane hydrate-bearing sediments. We prepared hydrate-bearing sediments with 10% fines content and 20–40% methane hydrate saturation, and depressurized those samples while acquiring CT images. The salient findings of this study are as follows:

1. The spatial evolution of free gas generation was captured and visualized using CT data during depressurization. Then, using the spatial information on gas bubbles, local changes in fines content (FC) during depressurization of the samples was successfully tracked after proper calibration with the post-experiment sampling results. Based on CT images, it appears that FC changes started occurring from the regions where methane hydrate dissociated; hence, this confirms that the multiphase fluid flow caused by depressurization accompanies fines migration.
2. In all samples, FC removals from ~10% to ~6–9% were caused by depressurization of hydrate-bearing sediments. The extent of fines migration differed with the particle sizes of the host sands and the types of fines; ~2–4% FC change for coarse sand with some silts, ~1–2% FC change for fine sand with some silts, and ~0.5–1% FC change for fine sand with some clays. Despite the limited number of samples tested, our results support the hypothesis that an increase in the pore size of host sands and a decrease in plasticity of fines cause more fines migration.
3. The-order-of-magnitude estimation using the Kozeny–Carman model reveals that the observed FC removal of 1–4% may increase sediment

permeability by a factor of 1.3–3.6, and such permeability increase can be as large as by a factor of 10 with the FC removal of 6–7%.

4. Hydrate plugging was enhanced in the presence of clay minerals. It indicates that the pore clogging phenomenon is affected not only by the degrees of hydrate saturation and fines content but also by the characteristics of fines. Thus, the physical properties of the sediments at the site and the relevant fines migration need to be investigated to identify optimum depressurization strategies.

#### Acknowledgments

We would like to thank Associate Editor Dr. Carolyn Ruppel and two anonymous reviewers for providing valuable comments and suggests, which was very helpful to improve this manuscript. All of the X-ray CT images and acquired data used in the figures are archived in the website (kwon.kaist.ac.kr) and Digital Rocks Portal ([www.digitalrocksportal.org](http://www.digitalrocksportal.org)) with the project name Fines migration in sediments containing methane hydrate during depressurization.' (doi:10.17612/P7R377). These data can be also requested by e-mail (t.kwon@kaist.ac.kr). This research was supported by the Korea Institute of Energy Technology Evaluation and Planning (KETEP) and the Ministry of Trade, Industry and Energy (MOTIE) of the Republic of Korea (20152520100760), by a grant (17CTAP-C129729-01) from Technology Advancement Research Program (TARP) funded by Ministry of Land, Infrastructure and Transport of Korean government, and by the Ministry of Trade, Industry, and Energy (MOTIE) through the Project “Gas Hydrate Exploration and Production Study” under the management of the Gas Hydrate Research and Development Organization (GHDO) of Korea and the Korea Institute of Geoscience and Mineral Resources (KIGAM).

#### References

- Abegg, F., Bohrmann, G., Freitag, J., & Kuhs, W. (2007). Fabric of gas hydrate in sediments from hydrate ridge—Results from ODP leg 204 samples. *Geo-Marine Letters*, 27( 2–4), 269– 277. <https://doi.org/10.1007/s00367-007-0080-4>
- Bedrikovetsky, P. (2008). Upscaling of stochastic micro model for suspension transport in porous media. *Transport in Porous Media*, 75( 3), 335– 369. <https://doi.org/10.1007/s11242-008-9228-6>
- Bedrikovetsky, P., Zeinijahromi, A., Siqueira, F. D., Furtado, C. A., & de Souza, A. L. S. (2011). Particle detachment under velocity alternation during suspension transport in porous media. *Transport in Porous Media*, 91( 1), 173– 197.
- Bergendahl, J., & Grasso, D. (2000). Prediction of colloid detachment in a model porous media: Hydrodynamics. *Chemical Engineering Science*, 55( 9), 1523– 1532. [https://doi.org/10.1016/S0009-2509\(99\)00422-4](https://doi.org/10.1016/S0009-2509(99)00422-4)

- Buffett, B. A. (2000). Clathrate hydrates. *Annual Review of Earth and Planetary Sciences*, 28( 1), 477- 507. <https://doi.org/10.1146/annurev.earth.28.1.477>
- Carman, P. C. (1937). Fluid flow through granular beds. *Transactions. Institute of Chemical Engineers*, 15, 150- 166.
- Cerda, C. M. (1987). Mobilization of kaolinite fines in porous media. *Colloids and Surfaces*, 27( 1-3), 219- 241. [https://doi.org/10.1016/0166-6622\(87\)80339-6](https://doi.org/10.1016/0166-6622(87)80339-6)
- Cerda, C. M. (1988). Mobilization of quartz fines in porous media. *Clays and Clay Minerals*, 36( 6), 491- 497. <https://doi.org/10.1346/CCMN.1988.0360602>
- Cha, Y., Yun, T. S., Kim, Y. J., Lee, J. Y., & Kwon, T.-H. (2016). Geomechanical, hydraulic and thermal characteristics of deep oceanic sandy sediments recovered during the second Ulleung basin gas hydrate expedition. *Energies*, 9( 10), 775. <https://doi.org/10.3390/en9100775>
- Cho, G. C., Dodds, J., & Santamarina, J. C. (2006). Particle shape effects on packing density, stiffness, and strength: Natural and crushed sands. *Journal of Geotechnical and Geoenvironmental Engineering*, 132, 591- 602. [https://doi.org/10.1061/\(ASCE\)1090-0241\(2006\)132:5\(591\)](https://doi.org/10.1061/(ASCE)1090-0241(2006)132:5(591))
- Collett, T. S., Lewis, R. E., Dallimore, S. R., Lee, M. W., Mroz, T. H., & Uchida, T. (1999). Detailed evaluation of gas hydrate reservoir properties using JAPEX/JNOC/GSC Mallik 2L-38 gas hydrate research well downhole well log displays. In S. R. Dallimore, T. Uchida, & T. S. Collett (Eds.), *Scientific Results from JAPEX/JNOC/GSC Mallik 2L-38 Gas Hydrate Research Well, Mackenzie Delta, Northwest Territories, Canada*, Bulletin Geological Survey of Canada (Vol. 544, pp. 295- 312).
- Davie, M. K., Zatsepina, O. Y., & Buffett, B. A. (2004). Methane solubility in marine hydrate environments. *Marine Geology*, 203( 1-2), 177- 184. [https://doi.org/10.1016/S0025-3227\(03\)00331-1](https://doi.org/10.1016/S0025-3227(03)00331-1)
- Freifeld, B. M., Kneafsey, T. J., & Rack, F. R. (2006). On-site geological core analysis using a portable X-ray computed tomographic system. *Geological Society of London, Special Publication*, 267( 1), 165- 178. <https://doi.org/10.1144/GSL.SP.2006.267.01.12>
- Gabriel, G. A., & Inamdar, G. R. (1983). An experimental investigation of fines migration in porous media, Society of Petroleum Engineers.
- Gupta, A., Moridis, G. J., Kneafsey, T. J., & Sloan, E. (2009). Modeling pure methane hydrate dissociation using a numerical simulator from a novel combination of X-ray computed tomography and macroscopic data. *Energy & Fuels*, 23( 12), 5958- 5965. <https://doi.org/10.1021/ef9006565>



- Ito, T., Komatsu, Y., Fujii, T., Suzuki, K., Egawa, K., Nakatsuka, Y., et al. (2015). Lithological features of hydrate-bearing sediments and their relationship with gas hydrate saturation in the eastern Nankai trough, Japan. *Marine and Petroleum Geology*, 66, 368– 378. <https://doi.org/10.1016/j.marpetgeo.2015.02.022>
- Jung, J., Cao, S. C., Shin, Y.-H., Al-Raoush, R. I., Alshibli, K., & Choi, J.-W. (2017). A microfluidic pore model to study the migration of fine particles in single-phase and multi-phase flows in porous media. *Microsystem Technologies*, 24( 2), 1071– 1080. <https://doi.org/10.1007/s00542-017-3462-1>
- Jung, J. W., Jang, J., Santamarina, J. C., Tsouris, C., Phelps, T. J., & Rawn, C. J. (2012). Gas production from hydrate-bearing sediments: The role of fine particles. *Energy & Fuels*, 26( 1), 480– 487. <https://doi.org/10.1021/ef101651b>
- Kempel, G., Goldsztein, G. H., & Santamarina, J. C. (2009). Particle transport in porous media: The role of inertial effects and path tortuosity in the velocity of the particles. *Applied Physics Letters*, 95( 19), 194103. <https://doi.org/10.1063/1.3263718>
- Kneafsey, T. J., Seol, Y., Gupta, A., & Tomutsa, L. (2011). Permeability of laboratory-formed methane-hydrate-bearing sand: Measurements and observations using X-ray computed tomography. *SPE Journal*, 16( 01), 78– 94. <https://doi.org/10.2118/139525-PA>
- Kneafsey, T. J., Tomutsa, L., Moridis, G. J., Seol, Y., Freifeld, B. M., Taylor, C. E., & Gupta, A. (2007). Methane hydrate formation and dissociation in a partially saturated core-scale sand sample. *Journal of Petroleum Science and Engineering*, 56( 1-3), 108– 126. <https://doi.org/10.1016/j.petrol.2006.02.002>
- Kozeny, J. (1927). Ueber kapillare leitung des wassers im boden. *Sitzungsberichte der Akademie der Wissenschaften in Wien*, 136, 271– 306.
- Kvenvolden, K. A. (1993). Gas hydrates-geological perspective and global change. *Reviews of Geophysics*, 31( 2), 173– 187. <https://doi.org/10.1029/93RG00268>
- Kwon, T. H., Oh, T. M., Choo, Y. W., Lee, C., Lee, K. R., & Cho, G. C. (2013). Geomechanical and thermal responses of hydrate-bearing sediments subjected to thermal stimulation: Physical modeling using a geotechnical centrifuge. *Energy & Fuels*, 27( 8), 4507– 4522. <https://doi.org/10.1021/ef3018699>
- Lee, J. Y., Kim, G. -Y., Kang, N., Yi, B. Y., Jung, J. W., Im, J.-H., et al. (2013). Physical properties of sediments from the Ulleung Basin, East Sea: Results from second Ulleung Basin gas hydrate drilling expedition, East Sea (Korea). *Marine and Petroleum Geology*, 47, 43– 55. <https://doi.org/10.1016/j.marpetgeo.2013.05.017>



Makogon, Y. (1997). *Hydrates of Hydrocarbons* (p. 482). Tulsa, OK: PennWell Books.

McDowell-Boyer, L., Hunt, J., & Sitar, N. (1986). Particle transport through porous media. *Water Resources Research*, 22( 13), 1901- 1921. <https://doi.org/10.1029/WR022i013p01901>

Miranda, R.M., & Underdown, D. R. (1993). Laboratory measurement of critical rate: a novel approach for quantifying fines migration problems. SPE 25432. Proceeding of the SPE Production Operations Symposium. Oklahoma City, OK, USA, 21-23 March.

Mitchell, J. K., & Soga, K. (2005). *Fundamentals of Soil Behavior* (p. 577). New York: John Wiley.

Moghadasi, J., Müller-Steinhagen, H., Jamialahmadi, M., & Sharif, A. (2004). Theoretical and experimental study of particle movement and deposition in porous media during water injection. *Journal of Petroleum Science and Engineering*, 43( 3-4), 163- 181. <https://doi.org/10.1016/j.petrol.2004.01.005>

Moridis, G. J., Collett, T. S., Pooladi-Darvish, M., Hancock, S., Santamarina, C., Boswell, R., et al. (2011). Challenges, uncertainties, and issues facing gas production from gas-hydrate deposits. *SPE Reservoir Evaluation & Engineering*, 14( 1), 76- 112. <https://doi.org/10.2118/131792-PA>

Moridis, G. J., Kowalsky, M. B., & Pruess, K. (2007). Depressurization-induced gas production from class 1 hydrate deposits. *SPE Reservoir Evaluation & Engineering*, 10( 5), 458- 481. <https://doi.org/10.2118/97266-PA>

Muecke, T. W. (1979). Formation fines and factors controlling their movement in porous media. *JPT*, 31( 2), 144- 150. <https://doi.org/10.2118/7007-PA>

Murphy, A., Soga, K., & Yamamoto, K. (2017). *A laboratory investigation of sand production simulating the 2013 Daini-Atsumi knoll gas hydrate production trial using a high pressure plane strain testing apparatus*. Paper presented at 9th international conference on Gas Hydrates, Denver, CO, USA, 25-30 June.

Oyama, H., Abe, S., & Sato, T. (2015). *Experimental study of mud erosion phenomena at sand mud alternate layer*. Paper presented at Eleventh Ocean Mining and Gas Hydrates Symposium, International Society of Offshore and Polar Engineers.

Pang, S., & Sharma, M. M. (1997). A model for predicting injectivity decline in water-injection wells. *SPE Formation Evaluation*, 12, 194- 201.

Park, J., & Santamarina, J. C. (2017). Revised soil classification system for coarse-fine mixtures. *Journal of Geotechnical and Geoenvironmental Engineering*, 143( 8), 1- 13.

- Rees, E. V. L., Kneafsey, T. J., & Seol, Y. (2011). Methane hydrate distribution from prolonged and repeated formation in natural and compacted sand samples: X-ray CT observations. *Journal of Geological Research*, 2011, 1- 15. <https://doi.org/10.1155/2011/791815>
- Rutqvist, J., Moridis, G. J., Grover, T., & Collett, T. (2009). Geomechanical response of permafrost-associated hydrate deposits to depressurization-induced gas production. *Journal of Petroleum Science and Engineering*, 67( 1-2), 1- 12. <https://doi.org/10.1016/j.petrol.2009.02.013>
- Scheidegger, A. E. (1960). *The Physics of Flow Through Porous Media* (p. 313). Toronto: University of Toronto Press.
- Sell, K., Saenger, E. H., Falenty, A., Chaouachi, M., Haberthür, D., Enzmann, F., et al. (2016). On the path to the digital rock physics of gas hydrate-bearing sediments – Processing of in situ synchrotron-tomography data. *Solid Earth*, 7( 4), 1243- 1258. <https://doi.org/10.5194/se-7-1243-2016>
- Seol, Y., & Kneafsey, T. J. (2009). X-ray computed-tomography observations of water flow through anisotropic methane hydrate-bearing sand. *Journal of Petroleum Science and Engineering*, 66( 3-4), 121- 132. <https://doi.org/10.1016/j.petrol.2009.01.008>
- Shapiro, A. A., Bedrikovetsky, P. G., Santos, A., & Medvedev, O. O. (2007). A stochastic model for filtration of particulate suspensions with incomplete pore plugging. *Transport in Porous Media*, 67( 1), 135- 164. <https://doi.org/10.1007/s11242-006-0029-5>
- Sharma, M. M., Chamoun, H., Sarma, D. S. H. S. R., & Schechter, R. S. (1992). Factors controlling the hydrodynamic detachment of particles from surfaces. *Journal of Colloid and Interface Science*, 149( 1), 121- 134. [https://doi.org/10.1016/0021-9797\(92\)90398-6](https://doi.org/10.1016/0021-9797(92)90398-6)
- Sherard, J. L., Dunnigan, L. P., & Talbot, J. R. (1984). Filters for silts and clays. *Journal of Geotechnical Engineering*, 110( 6), 701- 718. [https://doi.org/10.1061/\(ASCE\)0733-9410\(1984\)110:6\(701\)](https://doi.org/10.1061/(ASCE)0733-9410(1984)110:6(701))
- Sloan, E. D., & Koh, C. (2008). *Clathrate Hydrates of Natural Gases* ( 3rd ed., p. 752). Boca Raton, FL: CRC Press.
- Ta, X. H., Yun, T. S., Muhunthan, B., & Kwon, T. H. (2015). Observations of pore-scale growth patterns of carbon dioxide hydrate using X-ray computed microtomography. *Geochemistry, Geophysics, Geosystems*, 16( 3), 912- 924. <https://doi.org/10.1002/2014GC005675>
- Torres, M. E., Trehu, A. M., Cespedes, N., Kastner, M., Wortmann, U. G., Kim, J.-H., et al. (2008). Methane hydrate formation in turbidite sediments of northern Cascadia, IODP expedition 311. *Earth and Planetary Science Letters*, 271( 1-4), 170- 180. <https://doi.org/10.1016/j.epsl.2008.03.061>

- Uchida, S., Klar, A., & Yamamoto, K. (2016). Sand production model in gas hydrate-bearing sediments. *International Journal of Rock Mechanics and Mining Sciences*, 86, 303– 316. <https://doi.org/10.1016/j.ijrmms.2016.04.009>
- Valdes, J. R., & Santamarina, J. C. (2006). Particle clogging in radial flow: Microscale mechanisms. *SPE Journal*, 11( 2), 193– 198. <https://doi.org/10.2118/88819-PA>
- Van Olphen, H. (1963). *An Introduction to Clay Colloid Chemistry* (p. 301). New York: John Wiley.
- Waite, W. F., Santamarina, J. C., Cortes, D., Dugan, B., Espinoza, D. N., Germaine, J., et al. (2010). Physical properties of hydrate-bearing sediments. *Reviews of Geophysics*, 47, RG4003. <https://doi.org/10.1029/2008RG000279>
- Wan, J., & Tokunaga, T. K. (2002). Partitioning of clay colloids at air-water interfaces. *Journal of Colloid and Interface Science*, 247( 1), 54– 61. <https://doi.org/10.1006/jcis.2001.8132>
- Winters, W. J., Wilcox-Cline, R. W., Long, P., Dewri, S. K., Kumar, P., Stern, L., & Kerr, L. (2014). Comparison of the physical and geotechnical properties of gas-hydrate-bearing sediments from offshore India and other gas-hydrate-reservoir systems. *Marine and Petroleum Geology*, 58, 139– 167. <https://doi.org/10.1016/j.marpetgeo.2014.07.024>
- Xu, W., & Ruppel, C. (1999). Predicting the occurrence, distribution, and evolution of methane gas hydrate in porous marine sediments. *Journal of Geophysical Research*, 104, 5081– 5095. <https://doi.org/10.1029/1998JB900092>
- Yamamoto, K., Terao, Y., Fujii, T., Ikawa, T., Seki, M., Matsuzawa, M., & Kanno, T. (2014). Operational overview of the first offshore production test of methane hydrates in the Eastern Nankai Trough, 2014 Offshore Technology Conference, OTC-25243-MS, Houston, TX.
- You, Z., Yang, Y. L., Badalyan, A., Bedrikovetsky, P., & Hand, M. (2016). Mathematical modelling of fines migration in geothermal reservoirs. *Geothermics*, 59, 123– 133. <https://doi.org/10.1016/j.geothermics.2015.05.008>